UNIVERSIDAD
NACIONAL
DE COLOMBIA

Mechanical Behavior of Al_2O_3-13%TiO_2 Ceramic Coating at Elevated Temperature

Carlos Mario Serna Zuluaga

Universidad Nacional de Colombia

Facultad de Minas, Departamento de Materiales y Minerales

Medellín, Colombia

2016

Mechanical Behavior of Al_2O_3-13%TiO_2 Ceramic Coating at Elevated Temperature

Carlos Mario Serna Zuluaga

A thesis submitted in partial fulfilment of the requirements for the degree of:

M. Eng. Advanced Materials and Processes

Advisor:

Ph.D. Juan Manuel Meza

Co-advisor:

Ph.D. Alejandro Toro

Line of Research:

Ceramic Coatings

Research Group:

GTS Tribology and Surfaces Group

Universidad Nacional de Colombia

Facultad de Minas, Departamento de Materiales y Minerales

Medellín, Colombia

2016

Acknowledgements

This thesis work was carried out in the laboratories of the Tribology and Surfaces Research Group at Universidad Nacional de Colombia and the laboratories of the GIPIME Group at Universidad de Antioquia. The work was finally supported by Universidad Nacional de Colombia and the EPM Group (Empresas Públicas de Medellín E.S.P[1]).

First of all, I wish to express my sincere gratitude and appreciation to Professor Juan Manuel Meza for his tutoring and for helping me to complete this research; I am also grateful to my co-advisor, Alejandro Toro who was the one with whom this adventure started.

Even though this research is an individual work, I place on record, my sense of gratitude to one and all, who directly or indirectly, have lent their helping hand in this venture, because without them, I could have never explored subjects like those stated in this thesis.

Special thanks to: Tribology and Surfaces Group[2,3,4] (GTS) from the National University of Colombia, Pablo Gómez from EPM Group, Fabio Vargas and Edwin Cadavid from GIPIME Group (University of Antioquia); Juan Ospina, Augusto Barrios, Alexander Arboleda, Julián Ruiz, and David Acosta.

Last but not least, a very special thanks to my family and friends for the support they have lent me over the time I took to complete this research.

[1] http://www.epm.com.co/
[2] http://goo.gl/HlTtOb
[3] http://goo.gl/6YYY8E
[4] gtsunalmed@gmail.com

Abstract

The present thesis work has been carried out with the aim of studying the mechanical behavior of Al_2O_3-13wt.%TiO_2 ceramic coating (AT-13) at room and elevated temperatures. AT-13 coatings were deposited, with two different standoff distances (110 and 140 mm), by the flame spraying technique; their microstructure and composition were analyzed by means of optical and scanning electron microscopy and X-ray diffraction. The mechanical behavior of the coated systems was evaluated by means of tensile tests, micro- and nano-indentation techniques; the critical strain for cracking was found to be between 0.7 and 0.51% for both coatings, it was obtained in situ and recorded with the aid of a high resolution camera during tensile test at room temperature, as well as the cracking stages A (initiation), B (nucleation), C (propagation), and D (saturation), represented on the stress-strain curve. The strains relative to the cracking stages (in situ) were applied to the coatings, at elevated (~200°C), and evaluated ex situ, finding that the AT-13 coating systems studied here were prone to delamination due to the poor strain compatibility between the substrate and the bond coat. It was found that the degree of porosity, highly influenced the critical strain which was higher for the coating with the lower porosity, ε=0.70±0.08%, when compared to the coating with the higher porosity, ε=0.51±0.05%.

Keywords: (AT-13, Alumina-titania coating, Mechanical properties, Elevated temperature, Critical strain).

Resumen

El presente trabajo fue desarrollado con el fin de estudiar el comportamiento mecánico de recubrimientos cerámicos Al_2O_3-13wt.%TiO_2 (AT-13) tanto a temperatura ambiente como a alta temperatura. Recubrimientos cerámicos AT-13 fueron depositados utilizando dos distancias de aspersión de 110 y 140 mm mediante la técnica de proyección térmica por llama; su microestructura y composición química fueron analizadas mediante SEM y DRX. El comportamiento mecánico de los recubrimientos fue caracterizado mediante pruebas de tracción y las técnicas de micro- y nano-indentación; la deformación crítica para el agrietamiento se encontró entre 0.7 y 0.51% para ambos recubrimientos; obtenida in situ, y grabada con la ayuda de una cámara de alta resolución durante las pruebas de tensión a temperatura ambiente, así como las etapas de agrietamiento A (Iniciación), B (nucleación), C (propagación), y D (saturación), representadas en la curva de esfuerzo deformación. Las deformaciones relativas a las etapas de agrietamiento (in situ) fueron aplicadas a los recubrimientos a alta temperatura (~200°C) y evaluadas ex situ, encontrando que los recubrimientos AT-13 estudiados en este trabajo fueron susceptibles a delaminación como consecuencia de la baja compatibilidad a la deformación entre el sustrato y la capa de anclaje. También se encontró que el grado de porosidad influencia el esfuerzo crítico que resultó ser mayor para el recubrimiento con la menor porosidad, ε =0.70±0.08%, al ser comparado con el de mayor porosidad, ε=0.51±0.05%.

Keywords: (AT-13, recubrimiento de alúmina-titania, Propiedades mecánicas, alta temperatura, Deformación crítica).

Table of contents

List of figures

List of tables

Introduction

The AT coating systems, Al_2O_3-TiO_2, deposited by the flame spraying technique, as well as other coating systems deposited by means of different deposition processes, represent a great challenge when it comes to assessing their mechanical performance at room and elevated temperatures, mainly because of the large number of parameters involved in the production processes, and the dimensions and condition of the substrate. The purpose of this writing is to contribute to gathering important knowledge that will be useful for the life cycle assessment of ceramic coatings deposited by thermal spraying techniques.

The world of coatings is very broad, and the deposition techniques used to produce them are many, this without mentioning their applications which are plentiful and focused on improving aspects like functional performance, service life and component cost. The evolution of ceramic coatings, see Figure 1-1, began its persistent breakthrough since the times of the First World War (1914-1918) and the Second World War (1939-1945) where the protection of metallic engineering materials was a topic of interest due to the need of resistance to high cycle temperatures, high cycling forces, sliding, erosion and corrosion on engine parts and weapons. During these periods, the usage of materials, such as glass and its derivates, with low thermal conductivity was taken as thermal protection, but factors like the cost of processing, the low expansion rate and the lack of strength made glass not to be a good material for this purpose [1].

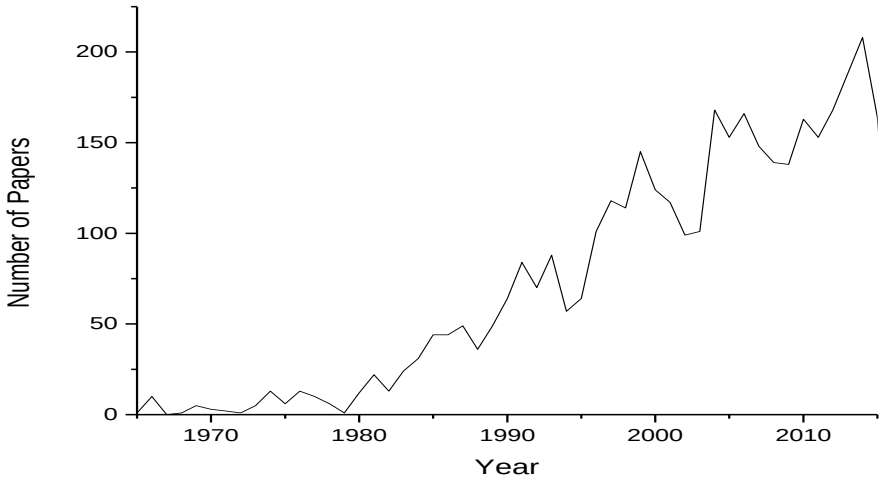

Figure 1-1. Historical evolution of ceramic coatings (documents by year) [2].

The publication “Review of an investigation of ceramic coatings for metallic turbine parts and other high-temperature applications” [3] could be the seminal paper about protection against high-temperatures by using a coating, and its aim was the development of ceramic coatings to protect and enhance the lifetime of alloys used in turbines. Hereupon, during the ‘50s the use of ceramic materials in engines began its climbing, but yet still fewer applications were found. During the ‘60s, the demand for ceramic coatings was increased thanks to the development of gas turbines where the metals and different alloys were not capable of bearing the high-temperature environments [4].

In recent years, there have been great improvements in analyzing the degradation behavior and the reliability of ceramic coating systems, but there is still some deficit in the capability for predicting damage evolution in terms of crack initiation and crack growth, which ultimately leads to macroscopic delamination and spallation of the coating system. A fundamental understanding of the damage evolution processes under different conditions such as isothermal, thermo-cyclic and thermo-mechanical loading conditions has to be developed [5].

Any contribution to the knowledge of the mechanical behavior of ceramic coatings at elevated temperatures is of great importance, either for the enhancement of

materials service life and for environmental reasons. The proposal of new approaches, new models or validation of existing analytical models with a pragmatic application are needed to get a benchmark for the prediction of components life time, and for the development of new modified coatings that will permit the endurance under operating conditions such as high temperature and tough environments.

This thesis proposes a protocol for the measurement of the mechanical properties of ceramic coatings in general, at room and elevated temperatures; it will be applied to the AT-13 coating system.
In order to achieve the main goal of this work, a re-design of a classical Monsanto tensometer, was performed to provide the capability of performing tensile tests at high temperatures, up to 1200°C.
The samples for the tensile test were designed based on the standard ASTM E8 [6] having a dog-bone shape. In order to assure a plane stress state, the design of the samples was verified by the finite elements method.
One of the difficulties faced on this work, apart from the costly experimentation was the usage of cold grips for performing the tensile tests at elevated temperature.

The content of this thesis starts with the chapter 1 “Ceramic coatings” which gives general information concerning to this topic such as the basic structure of a coating system and the materials with which it is produced, the spraying techniques used for its production, and finishes with the general properties of the ceramic coatings, fundamentals and testing. The chapter 2 “Materials and methods” gives the necessary information for unbiased future evaluation and reproducibility of the evaluation of the coating system. The chapter 3 “Results” explains the main outcomes of this study. The chapter 4 “Conclusions and recommendations” states the facts found during the entire work and lays feasible future work on the specific area covered here in. Additional information can be found in the appendices chapters.

Objectives

General objective

Evaluate the mechanical behavior of Al_2O_3-13 wt.% TiO_2 ceramic coating deposited by flame spray when submitted to elevated temperatures.

Specific objectives

- Characterize the Al_2O_3-13 wt.% TiO_2 ceramic coating for morphology, phase composition and properties by technics such as optical and SEM microscopy, and X-ray diffraction.
- Study the crack evolution of the coated system by means of in situ micro-tensile tests at room temperature.
- Correlate the ex situ cracking patterns of the coated system measured after elevated temperature tensile test with the in situ measurements obtained at room temperature.
- Measure the mechanical stiffness of the coated system by means of micro-tensile test at high temperature.

1 Ceramic Coatings

Ceramic coatings are usually applied onto structural metallic components to give them protection against corrosion, wear, erosion and to provide lubrication and thermal insulation. Coating systems such as alumina-titania, Al_2O_3-13wt%TiO_2, (AT-13) are commonly used to improve wear-, corrosion-, and erosion-resistance of steels [7], among other applications.

Figure 1-1 shows the typical surface morphology and the structure at the cross-section of Al_2O_3-TiO_2 coatings, where the metallic substrate, bond coat and top ceramic coat compose the ceramic coating system.

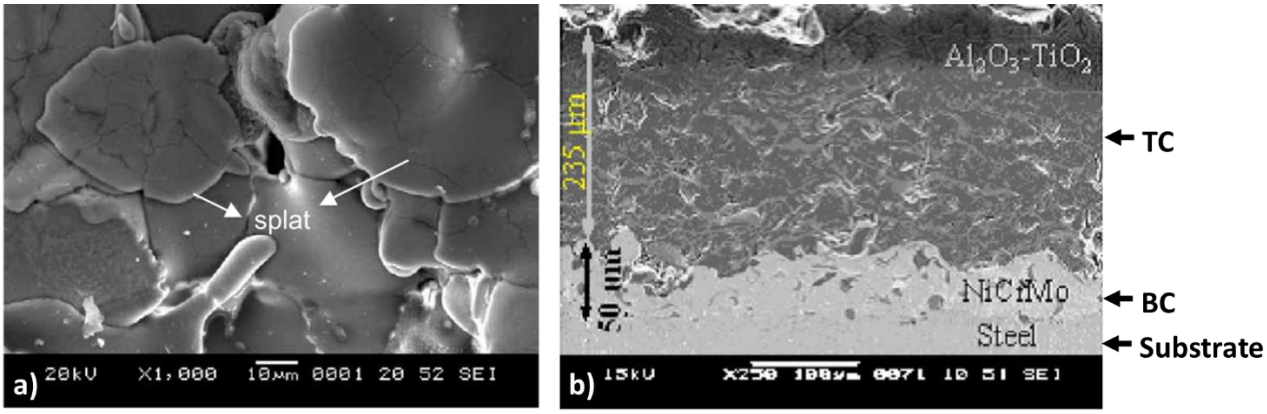

Figure 1-1. Typical surface morphology and cross-section structure of Al_2O_3-TiO_2 coatings [8].

These coatings are usually applied by techniques such as thermal spraying because it is necessary to achieve temperatures high enough to melt the ceramic material to form the coating; thermal spraying process is widely used to make thick

coatings for various industrial applications [8]. Additionally, ceramic coatings which are applied to reduce heat transfer may be divided as thin coatings (up to 0.5 mm) and thick coatings (up to 5-6 mm). Thin ceramic coatings are used in gas turbines, piston tops, cylinder heads and valves of auto and diesel engines [9]; while thick ceramic coatings are used in static engine components like turbine vanes and combustors, and can be used for abradable blade outer air seals [10].

1.1 Components of the ceramic coating system

The choice of a thermally sprayed material for an application is more complex than selecting a wrought or cast material for the same application because coating properties are not as predictable as those of conventional materials, however, the optimal pairing of the base material and the surface coating properties allows the obtention of characteristics and properties that would not be possible with homogeneous materials [11].

1.1.1 Substrate material

High strength aluminum alloys such as AA7075 can potentially be used instead of high strength steel to achieve weight reduction in different applications [12], but under high temperatures a significant growth of the precipitation particles is observed; for the alloy AA7075 it already starts at about 120°C [13]. In this ageing stage, the atoms of the alloy, which are in oversaturated solution produce minor precipitations by diffusion increasing the strength of the material. Artificial ageing temperatures normally vary between 100 and 200° C [14].

In terms of the effect of temperature on the properties of AA7075-T6 substrates, Cavaliere and Squillace reported that the hardness of the AA7075-T6 after high temperature, caused by friction stir process (FPS), is within the range of 124 and 141 Hv; the drop in the hardness is as a consequence of the coarsening of precipitates (overaging); they also reported a drop of about 62% in the yield strength after the FPS with a respective diminishing of the elongation of about 64% [15].

Different authors have coated AA7075 aluminum alloys by different thermal spraying techniques:

Macedo et al, coated a AA7075-T3 by techniques such as HVOF and LVOF and reported that thermal spraying of AA7075 alloys is viable because the change in the substrate hardness, after the spraying process, is not significant [16].
Arsenault et al, studied the fatigue integrity of the AA7075 aluminum alloy with an arc sprayed protective coating, and reported that it is possible to provide high fatigue resistance to metallic coated AA7075-T6; coated and uncoated substrates exhibited similar fatigue resistance [17].
Mourad et al, deposited cermets by means of HVOF technique onto a 7075-T6 substrate, and did not report any negative effect on the substrates [18].
Barbosa et al, have utilized the technique of Cold Spray to deposit Titanium coatings onto AA7075-T6 alloys [19]; in Cold Spray, the gas stream that exits the nozzle has relatively low temperatures (300 up to 800°C), and consequently the temperature of the particulate material remains below its melting point and therefore the resultant coating is formed in the solid state.
Ambiger and Kumar deposited alumina and zirconia coatings onto AA7075-T6 substrates by means of plasma spray technique to improve wear resistance of the aluminum alloy [20].

1.1.2 Bond coat (BC)

Bond coatings are widely used in many industrial spraying applications with the aim of providing a good thermal expansion match between substrate and ceramic coating [21], which in turn increases the resistance of the coating to the stress.

1.1.3 Top coat (TC)

The alumina-titania coating is conventionally used as hard coating due to its resistance to chemical and abrasive wear conditions [8], [22]. These coatings can

be used in applications where protection against abrasion, erosion, cavitation, wear, galling, fretting, friction, etc. is needed [11]. Alumina-titania coatings are usually manufactured by the atmospheric plasma spraying technique; coatings with a good adherence to the substrate and a low level of porosity can be produced under the high temperatures involved in the spraying process, [23], [24]. It is worthy to mention that oxides such as Al_2O_3 are classified among the ultra-high temperature materials [25].

1.2 Thermal spraying processes

Thermal spray is a technique that offers the possibility of producing a wide range of coatings for diverse applications [26]; it involves a variety of processes and materials. The deposition of a coating onto a substrate occurs when applying a stream of metallic or ceramic particles (wire or powder) in a flame or plasma jet to melt and accelerate them; after this, the particles flatten forming platelets called splats; by the application of several layers of these splats, the coating is formed [26], [27]. Different spraying techniques exist, but they are complementary and not competitive in the majority of cases i.e., an optimal spraying technique exists for a specific application [11]. The main objective of the thermal spraying technique is to increase the lifetime of materials by improving the performance of a component, adding functionality to surfaces. It is a very versatile technology that can be used in many types of applications and virtually almost on any component; it can be used against wear, corrosion, and aggressive and high-temperature environments, and for reparation and restoration of components [28], [22].

Figure 1-2 and Figure 1-3 show a classification of the thermal spraying processes and the temperatures and particle velocities obtained during the different processes; they are divided into two main groups: combustion and electric discharge [11], [28]. Each of these techniques differ mainly by the source of energy that is used to treat the material to be sprayed [29].

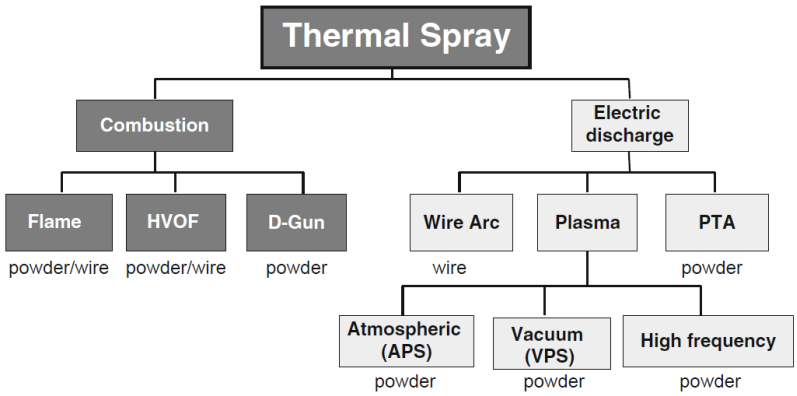

Figure 1-2. Classification of thermal spray technologies [11].

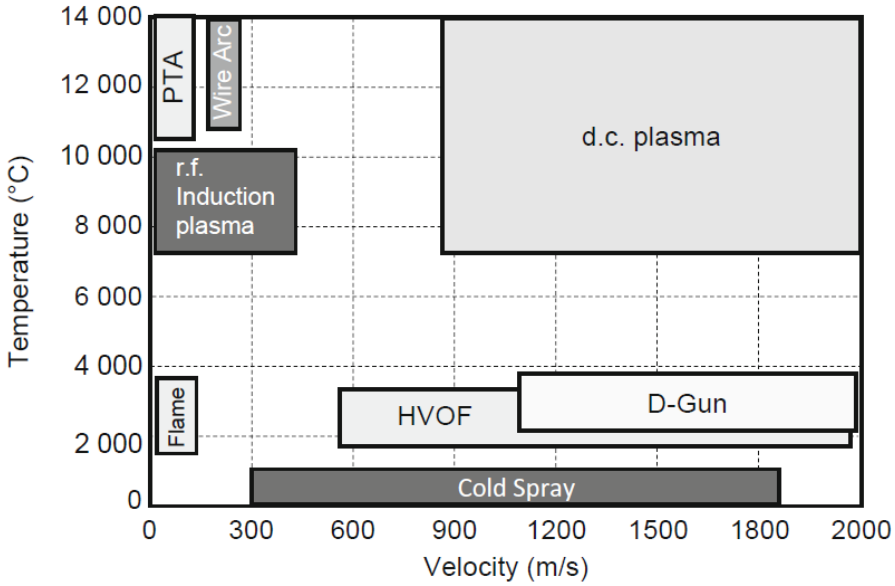

Figure 1-3. Gas temperature and velocities obtained with different thermal spray systems [11].

Thermal spraying is considered a potential alternative to traditional coating manufacturing techniques, such as hard chrome electroplating, for producing wear-resistant coatings [30]. The most commonly used thermal spraying processes for Al_2O_3-TiO_2 coatings are flame and plasma spraying [8], [24].

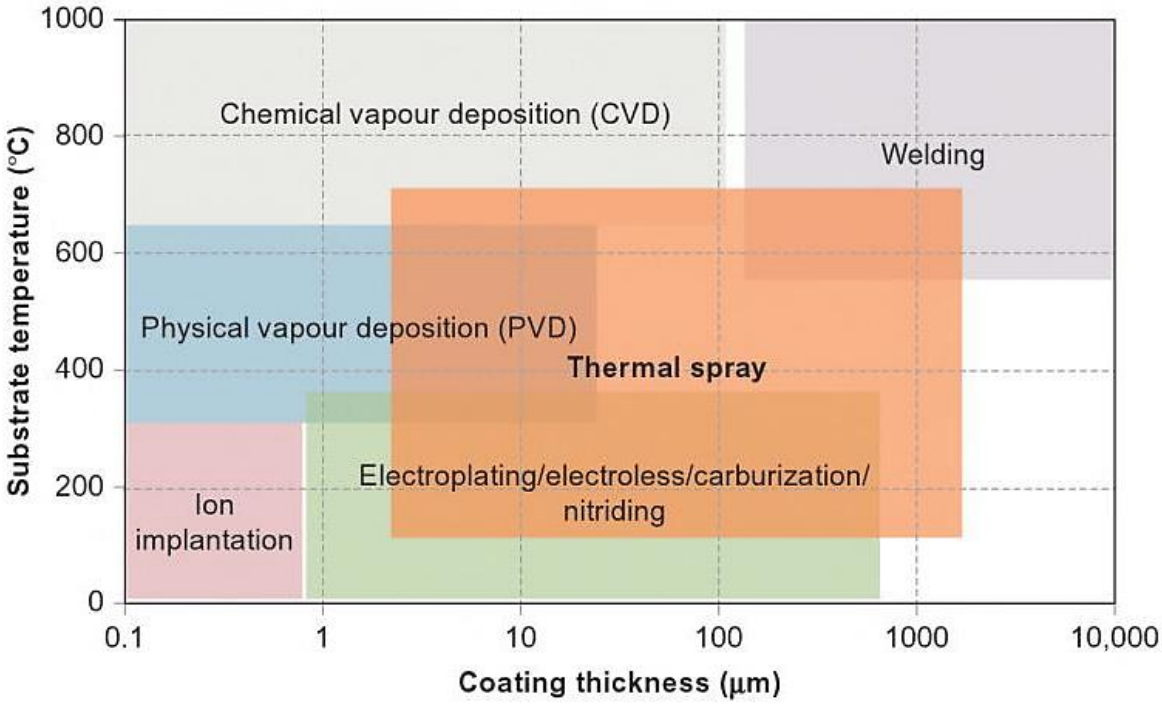

Figure 1-4. Comparison of different coating processes [28].

The differences among all coating properties and processes rely on the thickness, substrate temperature achieved during spraying, see Figure 1-4, and coating material.

Table 1-1. Thermal spray techniques comparison [28].

	Flame spray	Arc spray	Detonation gun	HVOF	APS	Cold spray
Flame/jet						
Temperature (°C)	3500	>6000	>4000	2500–3000	10,000–15,000	0–700 (preheated)
Velocity (m/s)	80–100	50–100	>2500	500–2000	300–1000	300–1200
Gas/fuel type	O_2/acetylene, propane, hydrogen	Air, nitrogen, argon	O_2/acetylene, hydrogen, propane, butane	O_2/natural gas, ethylene, propylene, propane, kerosene (liquid), hydrogen	Argon, helium, hydrogen, nitrogen and mixtures of them	Nitrogen, helium, air
Power input (kW)	20	5–10	–	150–300	40–200	–
Feedstock						
Max temperature in-flight (°C)	2500	>3800	–	3300	>3800	250
In-flight velocity (m/s)	50–100	50–150	750–1000	200–1000	50–100	500
Coating						
Porosity (%)	10–15 0 (for self-fluxing)	10–20	<2	<2	5–10	<5
Thickness (µm)	100–2500	100–2000	100–400	50–2000	100–1500	250–600

During the combustion thermal spraying, the coating material is melted in a flame that is generated by the combustion of fuel with oxygen; the melted material is

atomized by a compressed gas that propels the molten droplets onto a substrate to build up a coating, see Figure 1-5, [28], [31].

During the electric discharge thermal spraying, the introduction of an electric arc allows to get to higher temperatures, thus spraying of materials with higher melting points is possible [28].

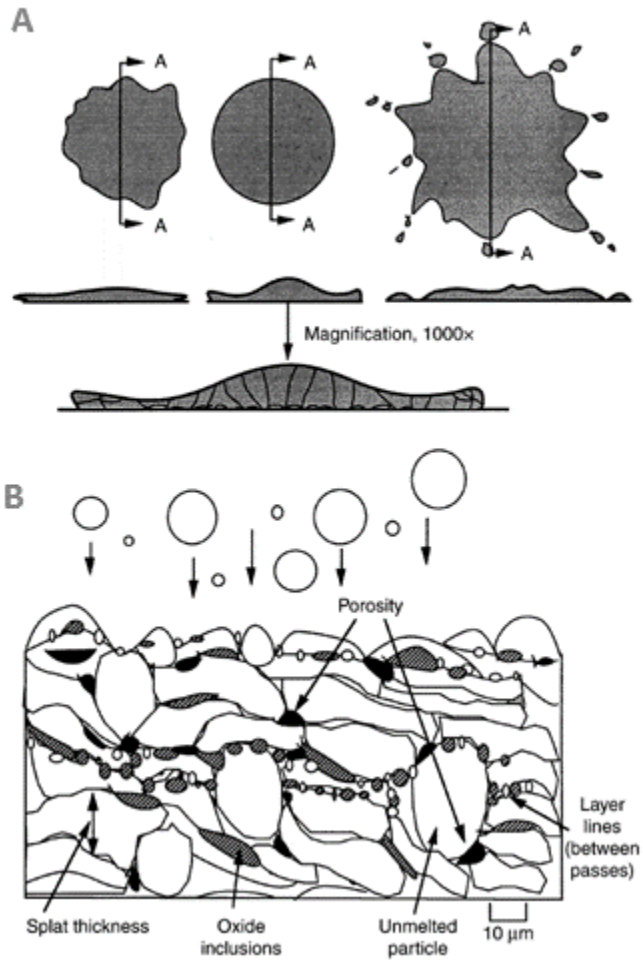

Figure 1-5. Typical morphology of the melted droplets; A) splat (or lamella) structure, B) common features [31].

Characteristics such as ceramic structure, adhesive strength, service life, thermal stresses in ceramic layer, and surface roughness are determined by the ceramic layer deposition technique. Coating service life and its performance depend not only

on its chemical composition but also on its structure and adhesive strength at the TC/BC interface [32], [33].

Coatings technology can be divided or classified into deposition of thin films (less than 20 µm) and deposition of thick films (>30 µm up to several millimeters). Thin films give an exceptional enhancement of surface properties; such is the case of chemical vapor deposition (CVD) or physical vapor deposition (PVD) that can provide surfaces with outstanding properties and corrosion resistance. Thick films are used when the component life depends on the layer thickness; thick film deposition methods include chemical/electrochemical plating, brazing, weld overlays, and thermal spray, among others [11].

Flame spraying, which belongs to the combustion thermal spray family, formerly called metallizing, is the oldest process, but it is still in common use [11]; it has been the basis for the development of more advanced techniques such as HVOF [28].
In flame spraying, oxyacetylene torches achieve premixed combustion temperatures up to about 3000 K. Spraying materials are introduced generally axially into the gun. Flame velocities below 100 m/s characterize this process [11].

High porosity levels influence negatively the material hardness (the lower the porosity, the higher the hardness, and vice versa) [9]. Slight variations in the amount of porosity, porosity type, average pore size, grain size, or grain size distribution may have a dramatic effect on mechanical, optical, thermal, and electrical properties of engineered materials [32].

Depending on the processing conditions and the structure of the feedstock, the coatings may exhibit different properties. The feedstock may be get in the form of powders, wires, cords and rods. The powder feedstock morphology and particle size distribution depend on their manufacturing route (atomization, fusing and crushing, milling and sintering, mechanical alloying and milling, spray drying, spheroidization, cladding, etc.)

1.3 AT-13 system

The Al_2O_3-TiO_2 system is an interesting material for obtaining tough ceramics, as well, it is well known for its excellent wear and corrosion behavior [34], and it is widely used in processes such as APS [22]. Titania is a material with a moderate wear resistance, fracture toughness, and hardness when compared to alumina; it can be easily thermal sprayed due to its relatively low melting point, 1855°C. Alumina-titania AT-13 have a higher melting point of about 2000°C. [24]. Alumina or alumina-titania coatings are fairly porous, a characteristic that can be an useful feature under harsh working environments [26].

Nanostructured ceramic materials show a superior resistance to wear, erosion, cracking and spallation [34], indeed, in literature it is agreed that nanostructured AT-13 coatings, made from nanostructured agglomerated powders deposited by APS exhibit a better performance to wear than the conventional AT-13 coatings (made from clad powders); nanostructured coatings are not harder than the conventional ones, but show a higher toughness which is considered to be the main characteristic that is responsible for their good wear performance [35].

1.4 Properties of ceramic coatings

The control of the in-service properties, of ceramic coatings, is sensitive to the large number of parameters involved in the deposition process, e.g., spraying process generally considers the effect of the energetic parameters that affect the flame properties such as enthalpy and velocity and consequently in-flight particle velocity and temperature during their flight, coating mechanical properties and consequently in-service properties [22]. The true mechanical behavior of the ceramic coating depends on different factors as methods for producing the powders, the final microstructure and size of the powders, and finally, the method used to project the powders onto the substrate.

1.4.1 Mechanical properties

The understanding of the mechanical behavior of ceramic coatings in both as-sprayed and thermomechanical loading conditions is of great importance for the components life prediction. However, it is challenging to determine the true mechanical behavior because of the substantial differences between each layer, (TC, BC, and substrate). Notwithstanding that the mechanical properties depend, as for any other material, on temperature, section thickness, deformation characteristics, phase stability under long-term high-temperature exposure, thermal cycling, and pollutants that can infiltrate the pores changing the mechanical behavior [19], [35].

Failure of most bodies occurs by the propagation of cracks during service conditions, such cracks may be present in the body from manufacture, so that for a successful design of coatings or layers with optimum properties, the general character of stresses should be known, and also how these stresses depend on various factors such as the thickness and mechanical properties of each layer [36].

Features like microstructure, chemical and phase composition, porosity and micro-crack pattern, coating thickness, adhesion to the substrate (and/or bond coat), and residual stresses influence the performance of ceramic coatings. In general, residual stresses are detrimental for the mechanical behavior, in fact, residual stresses are associated with the primary failure mechanisms (cracking and spallation), and influence the adhesion strength and the resistance to thermal and mechanical loading conditions. The actual residual stresses result from the quenching of the deposits during thermal spraying and the secondary cooling, which occurs when the ceramic system mismatches as a result of thermal cycling during service [37], [38].

Residual stresses may be divided into two broad categories: intrinsic stresses and thermal stresses. Intrinsic stresses may arise from compositional variations,

structural changes or defect generation in the microstructure, and they can play a significant role.

The thermal stresses during the spraying process are quite complex and they can be present as a stress gradient throughout the thickness; its significance depends on the type of cycling that is experienced by each component of the coating. The shrinkage of splats is caused by the quenching stresses that are tensile in nature, i.e., as the splat cools further after solidification, its thermal contraction is constrained by the underlying solid, developing the quenching stress (tensile) in this fashion [37], [39], [40], and it occurs due to the cooling from the melting point (deposition temperature) to the substrate temperature. In addition, during the cooling from deposition temperature to room temperature exists a differential thermal contraction (DTC) stress that may be either compressive or tensile depending on the sign of the difference between the metal and ceramic thermal expansion coefficients. The DTC is triggered by the thermal expansivity mismatch between substrate and ceramic, and it is introduced as well by thermal shock or thermal cycling effects during operating conditions.
Residual stresses are modified by various relaxation and redistribution effects that occur as a result of creep and yielding, in addition to debonding and sliding at interfaces. There are also important effects on the stress of thermal cycling, especially when one constituent is metallic and when the temperature range is large enough to cause yielding [41].

Sofiane Guessasma et al, studied the effect of the injection parameters on the wear behavior of AT-13 plasma sprayed coatings under different spraying parameters using a Pin-On-Disk (POD) test [22].

Evans and Hutchinson studied the principles governing the thermomechanical integrity of multilayers as means for fail-safe design of coated systems; “The dissimilar nature of the constituents presents challenges concerning the

thermomechanical integrity and reliability, especially when at least one of the constituents is brittle" [41].

Zhu et al, said that the major failure mode for ceramic coatings, like the Thermal Barrier Coatings, under tension, is spallation and delamination of the ceramic coating, which results from the nucleation, propagation and coalescence of surface cracks and interfacial delamination [42].

Lima and Marple, evaluated the Vickers hardness and the fracture toughness of conventional AT-13 coatings deposited by APS; the Vickers hardness was carried out under a 300 g load and 15 s on the cross section of the coatings, and the fracture toughness was performed by indentations with a Vickers indenter at a 5 Kg load and 15 s. The reported values for Vickers hardness, 1080±58 is similar to the values reported by Westgard et al., Luo et al., and Pawloswski, also ~1000 Hv; fracture toughness, 14.0±2.5 $MPam^{1/2}$ [24]. The values of fracture toughness are highly influenced by the microstructure of the powders.
In conventional coatings, the well-defined splat boundaries provide easy crack propagation paths compared to the nanostructured coatings where nano-zones help to stop crack propagation increasing the fracture toughness in this fashion.

1.4.2 Elastic stresses in bimaterial plates

In the literature, simplified expressions can be found for very thin coatings, where the material properties and temperatures do not depend on the coordinates (x and y), and the stresses and strains depend only on z, and act only in the plane of the plate; the stresses perpendicular to this plane are zero. These simplified expressions cannot be applied to thick coatings because they do not take into account the coating stiffness and the possibility that the body will be deformed by residual stresses that are usually the outcome of differences in thermal expansion between coating and substrate that cause deflection or distortion of the body. Even if these deformations are small, the associated stresses can be considerable because shear stresses that are present in the interface grow with the coating

thickness and are the main reason why thick coatings are more prone to spalling than thinner ones [36].

1.4.3 Stresses caused by differences in thermal expansion

Most ceramics are brittle at room temperature, but not necessarily at elevated temperatures, as the temperature of a material is increased, it is generally found that the Young's modulus slowly decreases as follows:

$$E = E_0 - bTexp\left(\frac{-T_0}{T}\right)$$

Where E_0 is the Young's modulus at absolute zero, b and T_0 are empirical constants; T_0 is about half the Debye temperature (the temperature at which the elastic vibration frequency of the atoms in a solid is the maximum). The rapid decrease of the Young's modulus at high temperatures has been attributed to non-elastic effects such as grain boundary sliding, and grain boundary softening [43].

These stresses are present when the substrate temperature differs from the temperature at which the coating was produced, as well, after operation regimes at high temperature.

During cooling, after firing, the layer with higher thermal expansion coefficient tries to contract more, and the layer with lower expansion coefficient prevents it. As a consequence, stresses arise in the component. As long as the temperatures are high, these stresses can relax. However, below a certain temperature they remain in the body permanently [36].

1.4.4 Phase transformation

Mechanisms that are promoted by temperature, such as phase transformation, in the surface, layer along with volume change, also affect residual stresses [36].

"Cracking and decohesion events expected in a multilayer system can be predicted, subject to knowledge about residual stresses, their redistribution, and the external loads, as well as the interface response" [41].

For example, the delamination crack path in APS TBCs systems is usually observed at different locations near the TGO-layer: it can appear within the TC, or close to the TGO, or the interfaces TC/TGO, BC/TGO or within the TGO.
At first, micro-cracks that already exist in the as-sprayed condition grow after heat exposure and/or number of thermal cycles (the crack growth is correlated with the exposure time at high temperatures). Ultimately, macro-cracks, which are predominantly oriented in the lateral direction, parallel to the TC/TGO interface, appear and cause the consequent spallation of the TC. The probable path of macroscopic spallation of TBCs depend on the thermal and/or thermo-mechanical loading profiles [44], [45].

Under service condition, or thermomechanical loading, when cracks initiate and propagate in the TC, the coating would be prone to spallation or delamination and the operation becomes impossible due to safety regards. [46].

1.4.5 Interface fracture toughness

Micro-tensile tests have been utilized in experiments carried out at high-temperatures and this could be an exceptional means of testing the thermomechanical behavior of ceramic coatings at high-temperatures.

“It is well known that the failure of TBC systems under thermomechanical loading is very complicated because it is influenced by the thermal mismatch, interface roughness, creep, sintering and so on” [47].

1.4.6 Tensile test for ceramic coatings

One of the means to evaluate the mechanical behavior is uniaxial tensile test. The strain generated in the specimens during uniaxial loading remains uniform over its thickness ensuring that the obtained results are easy to interpret [48].

A useful method to study the mechanical behavior of films or coatings that are deposited on substrates is the measurement of the straining that occurs during uniaxial tension at which a sequence of events occurs such as primary cracks, increase of the transverse crack density, saturation point and film decohesion [49]. The whole coating would break into many small segments by the interface stress that is transferred as a consequence of the substrate deformation when loaded at tension, and there may be a little dissipation or release of the normal stress σ_{xx} along the tensile direction in coating, but the external load applied in substrate monotonically increases, which results in the increase of the normal stress in coating. Finally, more parallel cracks form on the coating surface, as shown in Figure 1-6 [50].

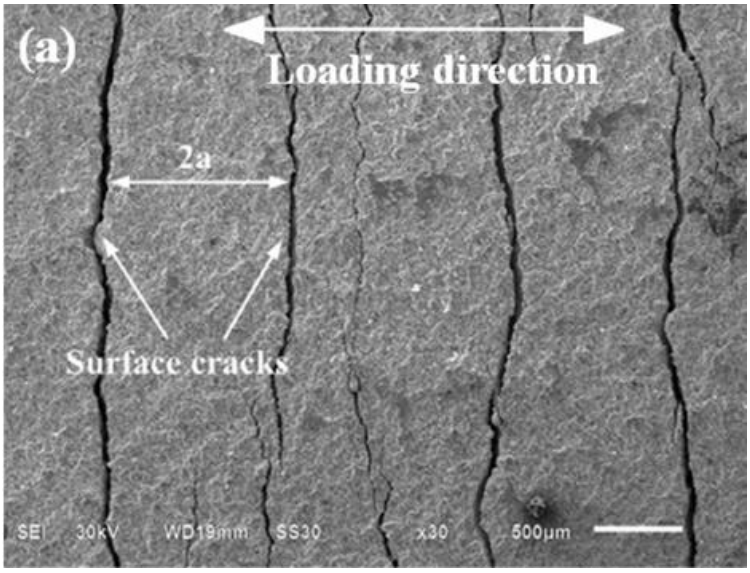

Figure 1-6. Multiple surface cracks observed under tensile loading [42].

Zhou, M., et al., investigated the failure behavior of APS TBCs, under uniaxial tension, by means of a coupled acoustic emission (AE) and digital image correlation (DIC) techniques to reveal the real-time damage evolution. They used a shear lag model to analyze the relationship between the vertical crack density on the coating and the applied strain in the substrate. Figure 1-7 shows a typical stress-strain curve of a coating system (substrate, BC, and TC); A, B, C and D show the representative

strain maps on the coating surface; these same points reflect the stages of cracking in the coating with the increase of the external strain in the substrate (initiation, nucleation, and propagation).

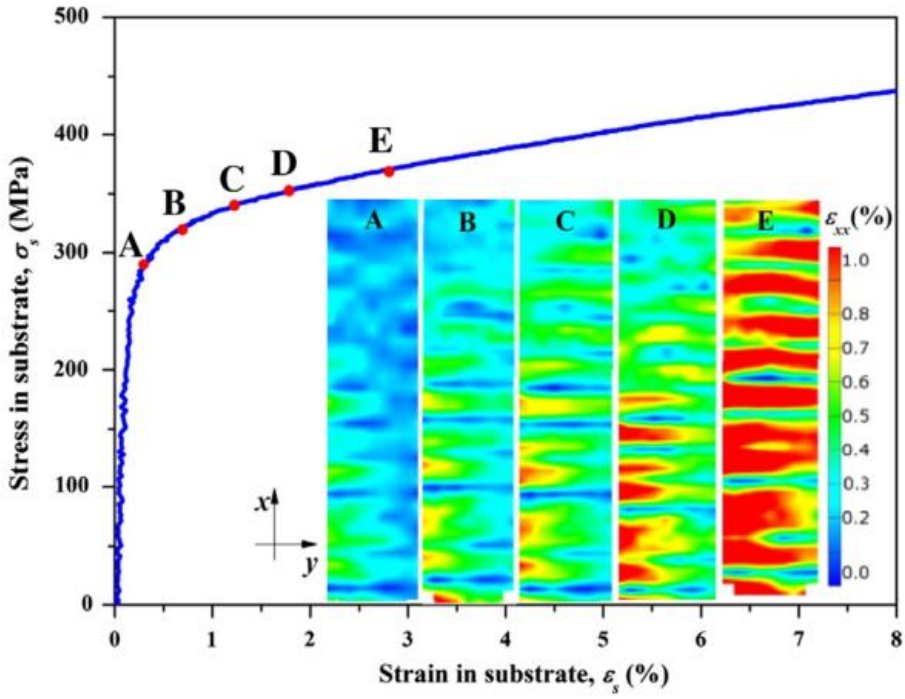

Figure 1-7. Typical stress-strain curve of TBCs under tension at room temperature [50].

During the initial stage (small ε_s) the coating undergoes transient elastic deformation; as strain increases, it is heterogeneously distributed (A); when the substrate deforms, from elastic to plastic, the strain concentration regions appear on the surface and gradually propagate perpendicular to the tensile (x-axis) direction; as strain increases further, some strain concentrations domains emerge on the surface (E) [50].

Zhou, M., et al. reported that the critical strain is found between 0.4 and 0.5% which is in agreement with Eberl, C. et al. who reported a critical strain for fracture in the TBC's top coat between 0.35 and 0.5%, which was measured in micro-beams test specimens [51]. This critical strain corresponds to the first stage of cracking, and other vertical cracks successively appear under the increasing tensile load, then, vertical cracks come to saturation. The effect of shear stress induced by the

substrate deformation on the coating gradually vanishes because all interface delamination comes to a saturation state.

Mao et al., following previous researches carried out by [52] and [53] (where uniaxial tensile tests were done at room temperature) studied the crack nucleation and propagation behavior of APS TBCs under uniaxial tension at room and high temperature, up to 1000°C, where the heating was achieved with help of an oxyacetylene torch towards TC surface. The test specimens, dog-bone samples, consisted of a plasma-sprayed 8wt.%YSZ TC, a NiCrAlY BC and a SUS304 stainless steel substrate [47].

Results reported by Mao et. Al., consisted of seven stages for the stress-strain curve of TBC specimens. Nucleation and propagation of transverse cracks correspond to the critical points P, A, B, C, D and E shown in Figure 1-8. The evolution of each transverse crack can be divided into three phases: initial cracking which occurs at A in the stress-strain curve, multiple transverse cracks which occurs between A and B, and crack saturation which occurs between B and C in the stress-strain curve.
In the C-D region the crack-crack spacing reaches a fixed-average space and delamination takes place.

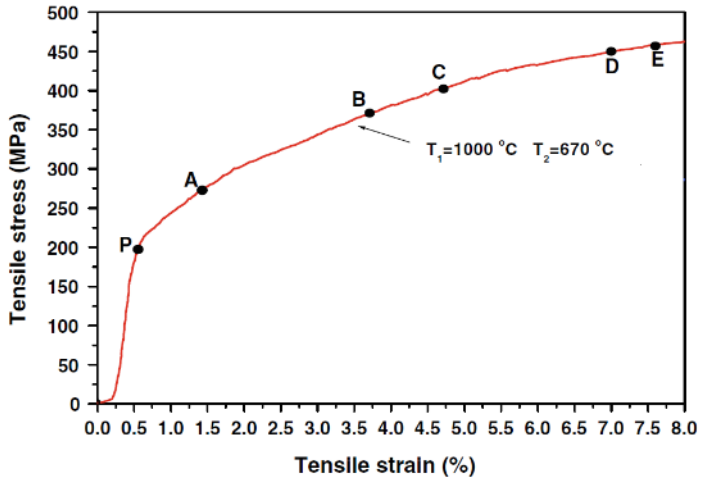

Figure 1-8. The tensile stress–strain curve of APS TBC system and its substrate material (stainless steel) at 1000◦C [47].

In the paper by Wu et al. TBCs samples deposited by EB-PVD with dog bone shape (Figure 1-9) were submitted to uniaxial tensile tests at different temperatures (20, 200, 400, 600, 800°C). Their results are summarized in Figure 1-9 and Figure 1-10, [54].

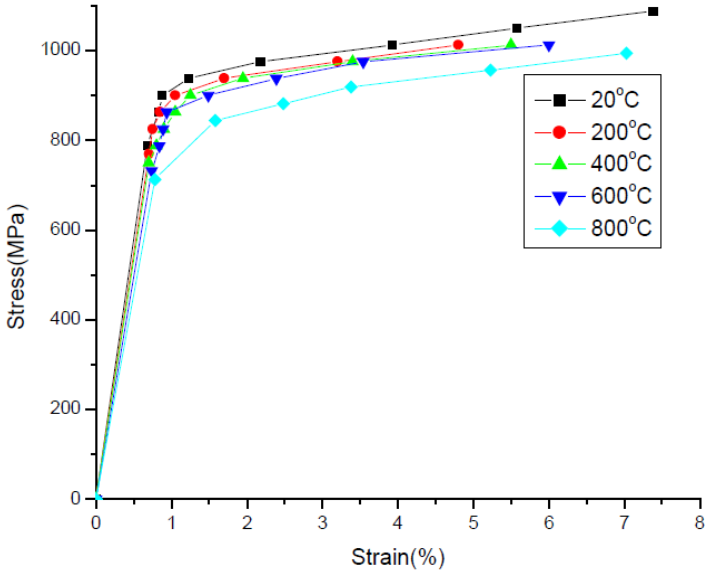

Figure 1-9. Stress-strain curves at different high-temperatures [54].

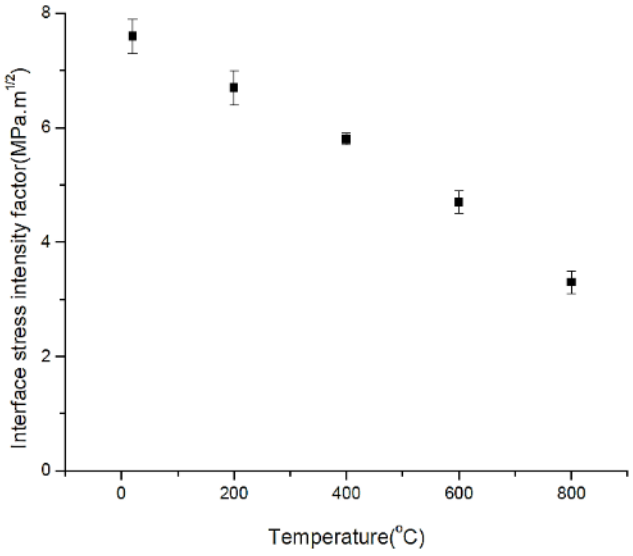

Figure 1-10. Stress intensity factors at high-temperatures [54].

The elastic modulus decreases about 80 MPa when temperature reaches 800°C; cracks which are normal to the loaded axis appear on the surface and saturate with the increasing strain. When the crack tip is close to the TC/BC interface, the crack kinks and propagates along this interface producing the spallation of the TC.
For the calculation of the stress intensity factors they have considered the thermal expansion mismatch and utilized the Suo-Hutchinson model which consider the interface cracking between two elastic layers, and have treated the bond coat and superalloy as a one single layer, hence the TBC system was composed of two layers. Basically, this model was based on the assumption that real bodies contain regions with different mechanical properties, then, the vicinity of a region with a different elastic modulus, and also the presence of an interface with a lower strength, have a pronounced influence on the behavior of a crack. Note that the stress state in such areas is much more complex than in homogeneous materials [36].

1.5 Weibull statistics

It is challenging to determine the true mechanical behavior of the ceramic coating because of the substantial differences, between each layer (TC, BC, and substrate). Weibull statistics is a method that offers good performance for extremely small samples, particularly for ceramic materials; this characteristic is important in areas such as aerospace industry (for safety problems) and in the development of testing methods with small batches, recall that for statistical relevance, larger batches are needed [55].

As it is well known, fracture in brittle solids usually occurs due to the existence of surface flaws or cracks that are in the presence of stress fields [56], when measuring properties of ceramic materials, a large scatteredness is observed; the same phenomena manifests in the top ceramic coat of ceramic coatings. The strain values, ε, (for cracking) of the TC present this scatteredness due to the

inhomogeneity and/or anisotropy of the ceramic coatings, their microstructure, size, shape, porosity, residual stresses, etc., so that a single value for strain is not a reliable parameter to predict the strain for fracture for ceramic coatings. According to Weibull statistics, the fracture will occur at the weakest place, so the application of this statistics for analyzing the fracture test data is a well recommended practice [56]. Weibull statistics, when applied to the fracture of brittle solids, refers to instantaneous failure at a particular applied stress [56].

Considering ε as a random variable which is a property that defines the crack extension (or crack stability), each value of ε has a certain probability of occurring which is given by the probability function $P(\varepsilon = x) = f(x)$. The cumulative probability distribution function for the random ε may be defined as $P(\varepsilon \leq x) = F(x)$, and yields the probability that ε takes on some value, less than or equal to x. The strain for fracture distribution may be described using the two-parameter Weibull probability distribution given by the following equation:

$$P(\varepsilon) = 1 - e^{-\left(\frac{\varepsilon}{K_0}\right)^m}$$

Where ε is the strain for fracture, and $P(\varepsilon)$ is its probability of occurrence (as an indicator of the weakest values); the Weibull modulus, m, indicates the scatteredness of the data, and K_0 is the characteristic strain for fracture or scale parameter (which is a value of the strain for fracture that includes 63% of the test data, when $\varepsilon = K_0$).

The Weibull probability distribution can be rearranged to a linear equation by taking two times its natural logarithm as follows:

$$lnln\left(\frac{1}{1 - P(\varepsilon)}\right) = mln\varepsilon - mlnK_0$$

The parameters, m and K_0, can be estimated by using different methods, but the most common is ordering/ranking statistics together with a linear regression. The strain for fracture values should be ordered from the smallest to the greatest, assigning each one a probability of occurrence based on its ranking, i, as follows:

$$P = \frac{i - 0.5}{N}$$

Where N is the total number measurements.

With the $P(\mathcal{E})$ and $\mathcal{E}$ values, Weibull plots are constructed as $ln\left[ln\left(\frac{1}{1-P(\mathcal{E})}\right)\right]$ vs $ln(\mathcal{E})$. Using the least square regression fit were used to calculate the values of m and K_0. Multiple flaw distributions may be further evidenced by deviation from the linearity of the data from a single Weibull distribution [57].

The Weibull modulus, m, and the characteristic strain for fracture, K_0, can be estimated by plotting $ln\left[ln\left(\frac{1}{1-P(\mathcal{E})}\right)\right]$ vs $ln(\mathcal{E})$ and taking a linear regression of the data points. The slope of the regressed line is the Weibull modulus, m, and its intercept is equal to $mlnK_0$. The graphical representation of this plot is useful for making judgements about the validity of the distribution function describing the data set. If the data points are clearly non-linear on such plot, then the distribution function probability does not adequately describe the behavior, which is an indicator of the presence of multiple defect distributions such as porosity, oxide films.

The scale parameter is calculated using $K_0 = e^{\left|-\frac{b}{m}\right|}$ where b is calculated as $-mlnK_0$, which is the intercept of the Weibull plot.

2 Materials and methods

This chapter deals with materials and steps required to produce and evaluate the behavior of the AT-13 coating systems at room and elevated temperatures. Elevated temperature is relative to the substrate, i.e., defined as ~40% of the melting temperature of the substrate. The chapter starts with the precursors, or raw materials, such as powders and substrates, then, the work itself is described from the thermal spraying technique with which the coated substrates were produced, and finishes with a brief description of the testing procedures and characterization techniques that were used during the study; the information contained herein is presented with the purpose of unbiased future evaluation and reproducibility.

The characterization of engineering properties out of ceramic coatings is a complex issue due to their inherent anisotropy and inhomogeneity. In terms of mechanical properties, testing methods may be mechanically simple in concept, but extremely sensitive to specimen preparation and test execution procedures. In order to study the mechanical behavior of the coated and uncoated substrates, characterization techniques such as stereo, optical and SEM microscopy, and X-ray diffraction were used to find information about composition, structure and microstructure of the samples.

2.1 Powders

In this work, AT-13 (Al_2O_3 - 13% wt.% TiO_2) conventional coatings were fabricated from commercial powders (METCO 6221, provided by OERLIKON METCO); these powders exhibit a spheroidal morphology consisting of agglomerated and sintered particles as shown in Figure 2-1. The nominal particle size distribution was between

25 and 48 µm, and a d(0.5) = 35.0 µm. The chemical composition of the AT-13 powders is shown in Table 2-1.

Table 2-1. Chemical composition of the AT-13 powders[5].

Product	Chemical Composition (nominal wt. %)						
	Al_2O_3	TiO_2	SiO_2 (max)	Fe_2O_3 (max)	MgO (max)	CaO (max)	Total all others (max)
Metco 6221	Balance	12.0-14.0	0.1	0.1	0.2	0.1	1.5

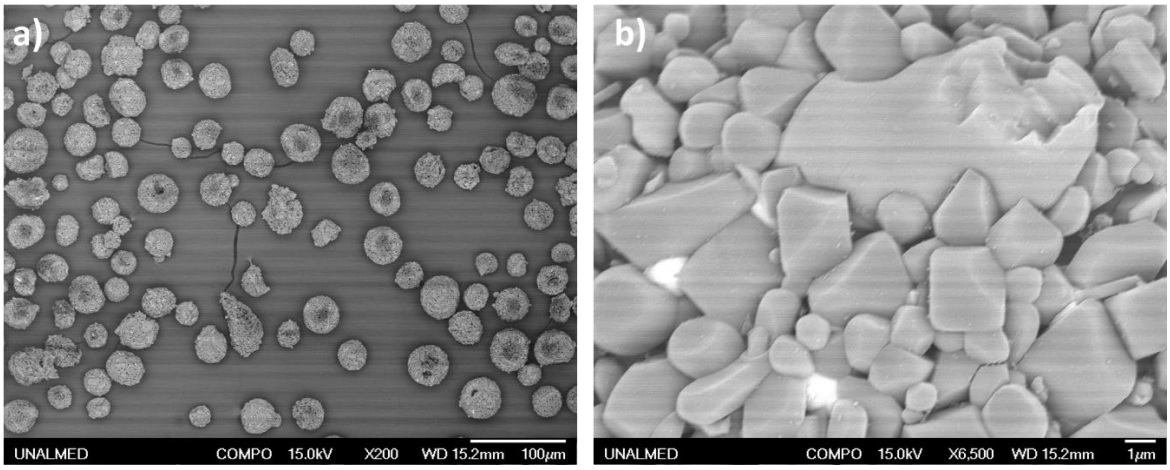

Figure 2-1. SEM images of AT-13 powders; a) General morphology, b) agglomerated components of a single particle.

The bond coating used to provide adhesion between the substrate and the top consisted of a NiCrAl type alloyed powders (Amdry 510, provided by OERLIKON METCO); these powders exhibit a spheroidal morphology as shown in Figure 2-2. The nominal particle size distribution was between 27 and 50 µm, and a d(0.5) = 37.0 µm. The chemical composition of the bond coat powders is shown in Table 2-2.

[5] http://www.oerlikon.com/ecomaXL/files/metco/oerlikon_DSMTS-0084.3_Al2O3_13TiO2.pdf&download=1

Table 2-2. Chemical composition of the bond coat powders[6].

Product	Chemical Composition (nominal wt. %)				
	Ni	Cr	Al	Others (max)	Organics (max)
Amdry 510	Balance	19.0-25.0	8.0-12.0	2.0	-

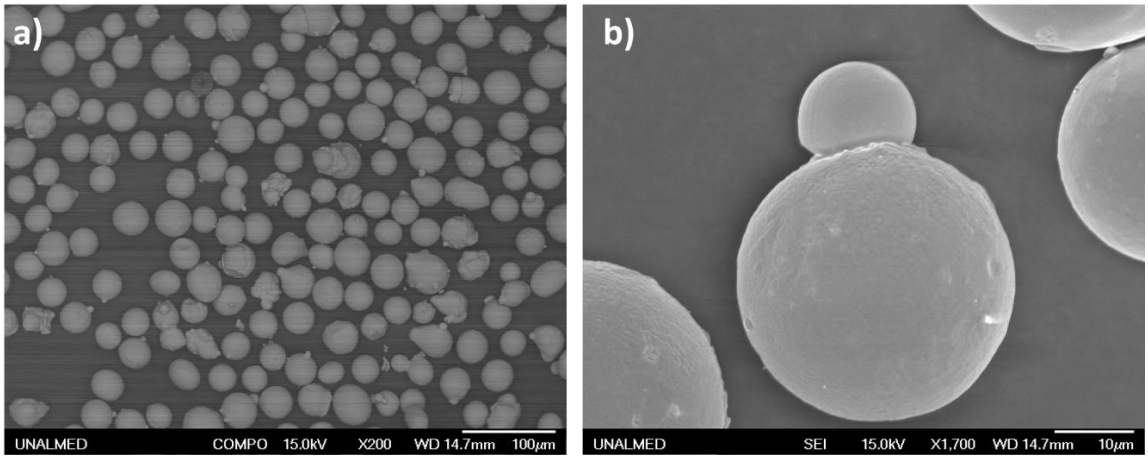

Figure 2-2. SEM images of bond coat powders; a) General morphology, b) single particle.

2.2 AA7075 Substrates

The material used as substrate consisted of an AA7075-T6 aluminum alloy which chemical composition is shown in Table 2-3. The chemical composition of the aluminum alloy was verified by means of atomic absorption spectroscopy.

Table 2-3. Chemical composition of the AA7075 aluminum alloy[7].

Product	Chemical Composition (nominal wt. %)			
	Zn	Mg	Cu	Others
AA7075	6.0	2.4	1.6	90.0

The substrates were previously dry blasted with a corundum powder up to a roughness of about 6.71±0.69 µm and cleaned in ultrasonic bath with isopropyl

[6] http://www.oerlikon.com/ecomaXL/files/metco/oerlikon_DSMTS-0091.4_NiCrAl.pdf&download=1
[7] ASTECO

alcohol in order to ensure the mechanical anchoring between the bond coating and the substrate.

Optical light microscopy, OM, observations were performed in the substrates before and after the thermal spraying process to evaluate its effect on the substrates microstructure. With the same aim, the Vickers hardness was measured (after and before the thermal spraying), according to the ASTM E384 standard and using a Vickers indenter with a 300 gf load for 10 s.

2.3 Deposition technique

The bond coat and top coat layers were deposited with the aid of an acetylene/oxygen flame with a ratio of 1:1.7, and the deposition was carried out with a TeroDyn System, see Figure 2-3 (Type 2000 spray coater, Eutectic Castolin - USA) facilitated by the GIPIMME research group from the Universidad de Antioquia, Colombia. The top coat layer was deposited using two different distances as stand-off parameter (110 and 140 mm). N_2 was used as carrier gas for the powders. The AT-13 powders were thermally sprayed over the BC surface. The spraying parameters of the bond coat (Amdry 510) and the top coat (METCO 6221) are summarized in Table 2-4.

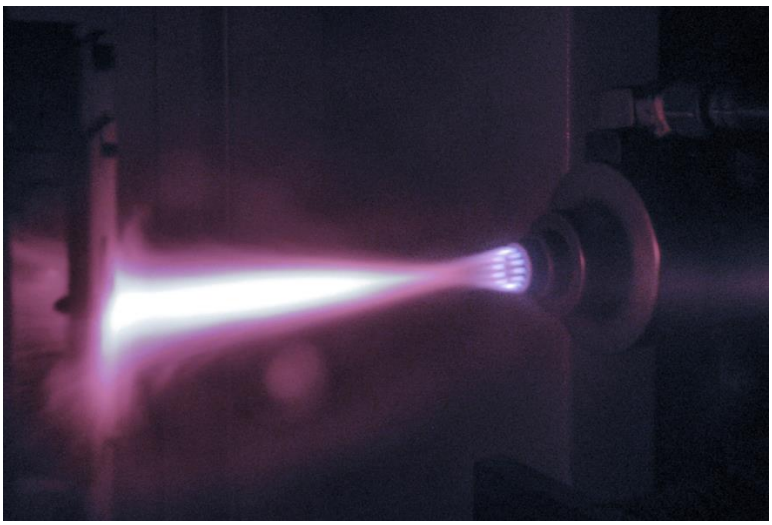

Figure 2-3. Flame spraying gun (TeroDyn system).

Table 2-4. Flame spraying parameters for both, the bond and the top coat.

SPRAYING PARAMETERS	**LAYERS**	
	BC (Amdry 510)	**AT-13** (METCO 6221)
Ratio acetylene/Oxygen	1:1.7	1:1.7
Powder feed rate g/min	25	13
Pressure Oxygen (PSI)	50 (37.4 L/min)	50 (40.8 L/min)
Pressure Acetylene (PSI)	12 (22 L/min)	12 (24 L/min)
Height Bille oxygen (mm)	38	40
Height Bille Acetylene (mm)	60	67
Spraying distance (mm)	150	**110 and 114**
Spraying angle	90	90
Substrate rotational speed (RPM)	116 (10%)	116 (10%)
Translational speed of the torch (cm/s)	0.72 (12%)	0.72 (12%)
Preheating passes	1	1
Spraying passes	4	5
Cooling allowed	YES	N/A

The final samples consisted of:

i) **AA7075-T6 Substrates**: Dog-bone-shaped with a cross-section of 25.96 ±0.15 mm^2 and a gage length of 25.4 mm.

ii) **AT-13 (110):** Dog-bone-shaped with a cross-section of 30.18 ±1.38 mm^2 and a gage length of 25.4 mm.

iii) **AT-13 (140)**: Dog-bone-shaped with a cross-section of 31.23 ±0.96 mm^2 and a gage length of 25.4 mm.

Figure 2-4 shows the dog-bone-shaped samples to be tensile tested at room and high temperatures. The structure and dimensions of the coatings are shown in the Results chapter.

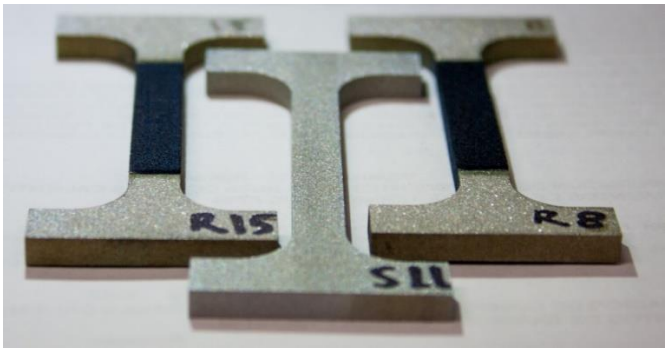

Figure 2-4. Dog-bone samples; AT-13 coating systems (left and right), AA7075-T6 substrate (center).

2.4 Re-design of a high temperature tensometer

A re-design of a classical Monsanto tensometer, was performed in order to be able of carrying out tensile tests at elevated temperatures. This equipment is instrumented with a gauge unit capable to measure strains with a resolution as low as 3 µm. To achieve high-temperatures, the specimen was heated by contact on the coating surface, with a MC-GAXP-30[8] spiral micro-heater, and the temperature measurement was carried out with contact thermocouples k-type. See Figure 2-5. More information can be found in Appendix A.

[8] The spyral microheater was bought at Micropyretics Heater International, Inc.

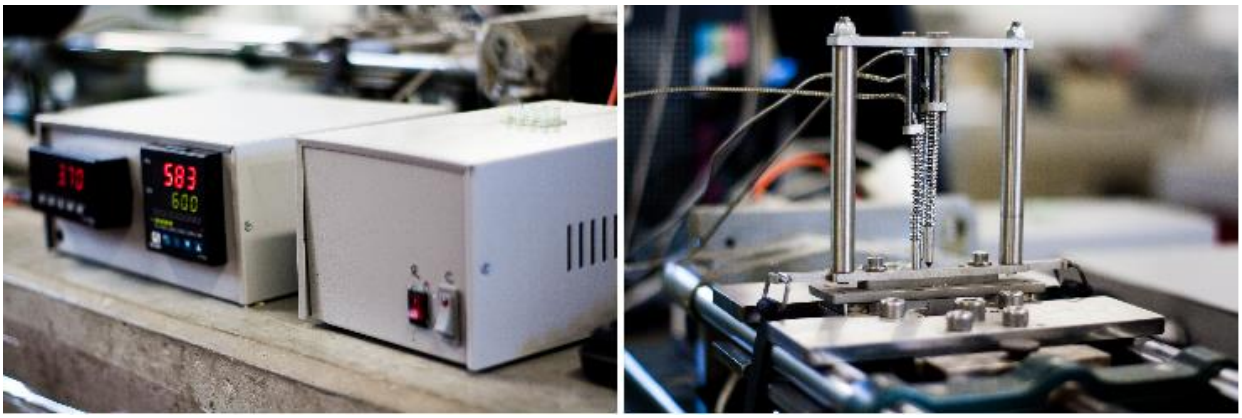

Figure 2-5. Monsanto tensometer instrumented and modified for high temperature testing.

2.5 Mechanical testing

2.5.1 Tensile testing

To in situ monitor the strain evolution of the samples during tension, at room temperature, a commercial white developer (aerosol paint, Spotcheck® SKD-S2) was sprayed on the as-sprayed coating surface. The selection of the developer was based on the best contrast achieved in trials with red penetrant dye, white developer and no stained samples (or as-sprayed).

The tensile tests were carried out with the tensometer described before; it was applied to both, uncoated and coated substrates; the Table 2-5 summarizes the samples distribution for the tensile tests.

Table 2-5. Samples used for the tensile tests.

	SAMPLES		
TEMPERATURE	**AT-13 (110 mm)**	**AT-13 (140 mm)**	**AA7075 Substrates**
25°C	4	4	4
~204°C	4	4	4

An 8.0-million-pixel device camera with super-macro function and sensor 1/2.5" type CCD was used to in-situ measure the macroscopic morphology and strain

evolution of the monitored region (6.5 x 25.4 mm^2) with a sampling rate of 30 FPS. The standard deviation, within a second, for the measurement of strains, was found to be 0.021%, i.e., in a specific second, the measured strain can get ±0.021% error. All experimental data are synchronized with the testing time. Four points A, B, C, and D where marked along the stress-strains curves of the AT-13 coating systems to highlight the crack initiation, nucleation, propagation, and saturation stages in the coatings, according to the increasing strain (born by the substrate).

During the tensile tests at elevated temperatures, as the heating is achieved by contact upon the TC's surface, it was not possible to in situ monitor the strain evolution, instead of this, each sample, during the high temperature tensile testing, was brought about the critical strain value (reported at room temperature), and the extent of the damage was ex situ analyzed on the polished cross-section by OM.

Figure 2-6. Elevated temperature setting.

The elevated temperature tensile test (Figure 2-6) consisted of a heating stage, 10 min heat-up from room temperature up to the desired temperature (25 up to ~204°C), (see **Error! Reference source not found.**), and 15 min holding time at t he high temperature.

2.5.2 Micro and nanoindentation

In order to evaluate the influence of the thermal spraying process in the substrates, the Vickers micro-hardness, before and after the thermal spraying, was measured with a Zwick-Roell at a load of 1000 gf for 15s, following the ASTM E384 standard.

The hardness and Young's modulus in the polished transversal section of the TC, BC and substrate were determined by nanoindentation test using an IBIS nanoindentation system and software (Fischer-Cripps Laboratories Pty Ltd.) equipped with a Berkovich tip indenter, following the Oliver and Pharr method. The Vickers hardness and Young's moduli were calculated from the load vs. depth curves after area correction. The maximum load was 500 mN; holding times to account for creep and thermal drift were used. To prevent the interference between the indentations, each indentation was kept separated from the previous one, at least five times the diagonal size. To ensure reproducibility of the results, a replica of each sample was also tested.

2.6 Characterization techniques

The techniques presented herein were used with the aim of characterizing the substrates and coated specimen's behavior before and after the thermal spraying deposition process, as well as after the tensile tests.

2.6.1 Surface roughness

The surface roughness of the gritted substrates, the sprayed BCs, and TCs were measured with a Mitutoyo SJ-20 where a stylus attached to the detector unit of the SJ-20 displaces at constant speed across the sample's surface, tracing surface irregularities. The chosen parameter for expressing roughness was Ra (arithmetic mean of the absolute values of the profile deviation from the center line).

2.6.2 Visible-light microscopy

The internal morphology of ceramic coatings contains different types of defects such as porosity and cracks; during metallographic preparation, a great deal of damage can be induced into the samples. Sectioning may cause localized cracking, delamination, or separation of the coating, as well, grinding and polishing. It is worth saying that during all the preparation steps for metallographic analyses some internal stresses may be released, and some others may be induced.
The cross-section of the AT-13 systems was examined, at 20X magnification using a visible-light microscope (Axio Scope A1 pol, Carl Zeiss, Germany), giving a quantitative and qualitative description of the coating structure.
The metallographic technique described herein was only used for the evaluation of the specimens' cross-section, and it was carried out with extreme care to avoid masklike readings. The steps in this technique were carried out following instructions found in the literature and given by the "Thermal Spray Accepted Practice Committees", and "the National Aeronautics and Space Administration (NASA)"; further information can be found in references [32], [59], [60], [61], [62], [63], [64], and [65].

All the samples were cold-mounted-vacuum assisted with a low-viscosity polyester, which is the most recommended mounting for thermal spray coatings, to achieve an effective penetration of the ceramic porous structure and diminish the mechanical damage during grinding and polishing. The vacuum impregnation was used as a critical method to preserve the coating integrity during subsequent preparation stages.

The substrates were prepared, before and after thermal spraying, by standard metallographic techniques and etched with Keller's reagent in order to evaluate the effect of the thermal spraying process on them.
The porosity measurement was carried out in accordance with the ASTM E2109 standard.

The mounted specimens were grinded following the surface preparation protocol described in Table 2-6.

Table 2-6. Metallographic procedure for ceramic coatings cross-section.

Step	Media	Carrier	Time (min)
1	240 grit	SiC paper	10
2	320 grit	SiC paper	10
3	400 grit	SiC paper	10
4	600 grit	SiC paper	10
5	600 grit	SiC paper	10
6	9 µm	Diamond on Synthetic hard cloth	10
7	6 µm	Diamond on Synthetic hard cloth	10
8	3 µm	Diamond on Synthetic hard cloth	10
9	1 µm	Diamond on Synthetic hard cloth	15

2.6.3 Scanning electron microscopy SEM

To examine the surfaces of the as-sprayed coatings the samples were inspected using a scanning electron microscope (SEM, JEOL JSM-5910 LV) equipped with BES and SEI detectors.

2.6.4 X-ray diffraction

The X-ray technique was used for the identification of the different phases that are present in the powders and coatings at room temperature. Phase characterization was conducted with a XPert PANalytical Empyrean Series II Diffractometer using a Cu Kα1/ Kα2 radiation (λ = 1.5406 Å) within a 20°< 2θ <80° range and step of 0.013°/70.7 seg. The software used for identification and quantification of the crystal phases was X'Pert High Score Plus Version 3.0c by PANalytical B.V. along with the database COD, using the Rietveld method as explained in appendix F. It is worth mentioning that the strong presence of defects in these materials creates a significant background noise.

2.7 Weibull statistics

The Weibull method was used to calculate the Weibull parameters, m and K_0, of the strain for fracture ε, data for the AT-13 coatings after being submitted to tensile tests at room temperature. The Weibull statistics was applied to the strain for fracture to obtain the probability of failure.

3 Results

3.1 Thermal spraying

3.1.1 Substrates

The chemical composition of the AA7075-T6 substrate was examined with a spark optical emission spectrometer Bruker Q8 Magellan; results are of a typical AA7075 alloy as it is shown in Table 3-1.

Table 3-1. Chemical composition of the AA7075 used as substrate.

AA7075 Chemical Composition (nominal wt. %)									
Al	**Zn**	**Mg**	**Cu**	Fe	Cr	Si	Mn	Ti	V
89.72	**5.901**	**2.431**	**1.175**	0.282	0.175	0.146	0.083	0.042	0.017

Sb	Ni	Zr	As	B	Pb	Sn	Co	P	Ca
0.011	0.0051	0.0047	0.0043	0.002	0.0012	<0.001	<0.001	<0.0005	0.00045

The microstructure of the AA7075 substrates in the as received and thermally sprayed conditions are shown in Figure 3-1; from Figure 3-1 a) is possible to see that the substrate in the as received condition, AA7075-T6, comprises a polycrystalline aggregate of grains and second phase particles; second phase particles can be divided into inclusions (constituent particles) with dimensions on the order of micrometers and precipitates with dimensions on the order of nanometers [66]. It is known that second phase particles affect the mechanical and corrosion properties of Al alloys [67]. The variation in mechanical and corrosion properties has been

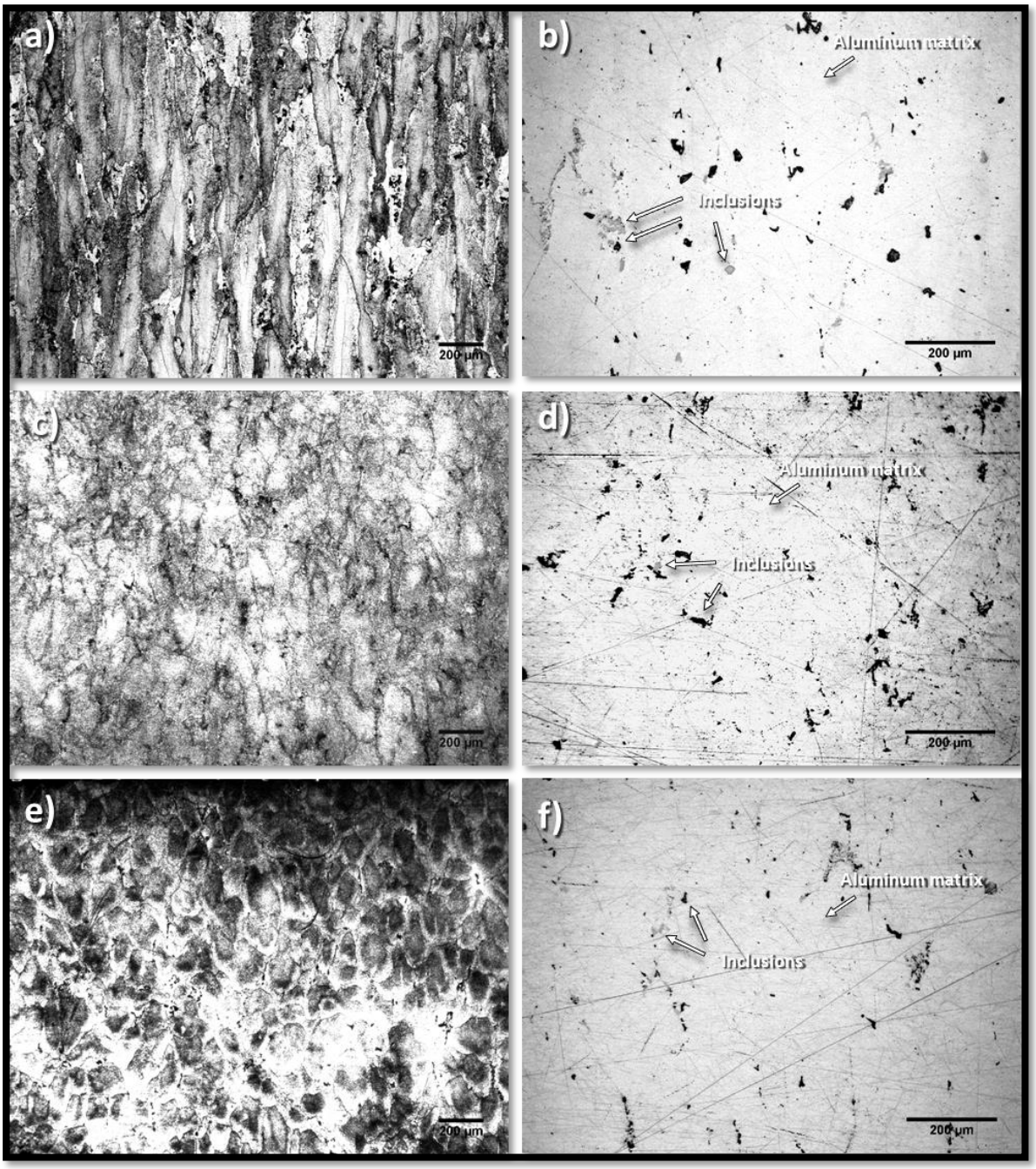

Figure 3-1. Microstructure of the substrates, in the as received and thermally sprayed conditions (grain structure at the left, inclusions at the right). (a, b) AA7075-T6; (c, d) AT-13 (110), and (e, f) AT-13 (140).

attributed to the size, shape, and distribution of precipitates in the alloy microstructure [66]. From Figure 3-1 c) and e) it is possible to see that the grain structure suffered a change after the thermal spraying processes, exhibiting recrystallized equiaxed grains; grains of the substrates that were thermally sprayed (Figure 3-1 c, e) look the smaller when compared to the as received condition (Figure 3-1 a). The changes of the grain structure are similar to those observed elsewhere after high temperature deformation of friction stir processed 7075 aluminum alloy [15].

No porosity or defects were observed in the samples, but second phases precipitated, and this may be explained by the fact that the material underwent a thermal treatment that promoted diffusion and rearrangement of defects, similar to an annealing-like treatment that softened the alloy. This is confirmed by measurements of hardness before and after the thermal spraying process.

The hardness values of the substrates, measured by micro- and nanoindentation techniques, are reported in Figure 3-2. The hardness showed a reduction of about 24.8% for substrates that were thermally sprayed at 110 mm, and 36.7% for substrates that were thermally sprayed at 140 mm with respect to the as received condition; the indentations performed by micro-indentation and nanoindentation techniques are shown in Figure 3-3. It is concluded that the thermal spraying process affected considerably the properties of the substrates as a consequence of a heat treatment caused during the thermal spraying, i.e., overaging promoted the softening of the substrates which in turn caused a loss of the mechanical properties of the substrates; this result is contradictory with some of those reported in the literature (see 1.1.1); The higher the temperature, during the spraying process, the smaller the grains in the after-sprayed substrates. In the thermo-mechanically affected zone the structure seems recrystallized, in all the after-sprayed substrates (Figure 3-1 B, and C).

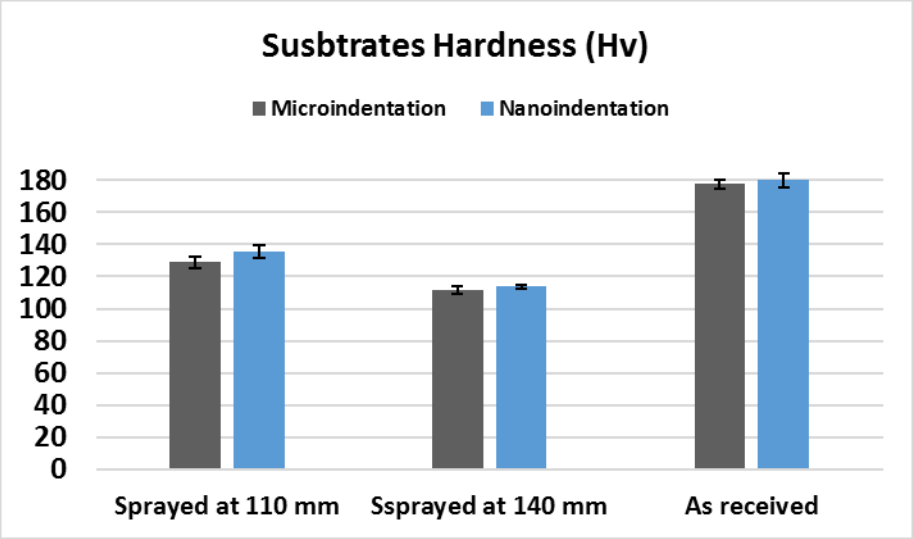

Figure 3-2. Hardness of the AA7075-T6 substrates in the as received and thermally sprayed conditions.

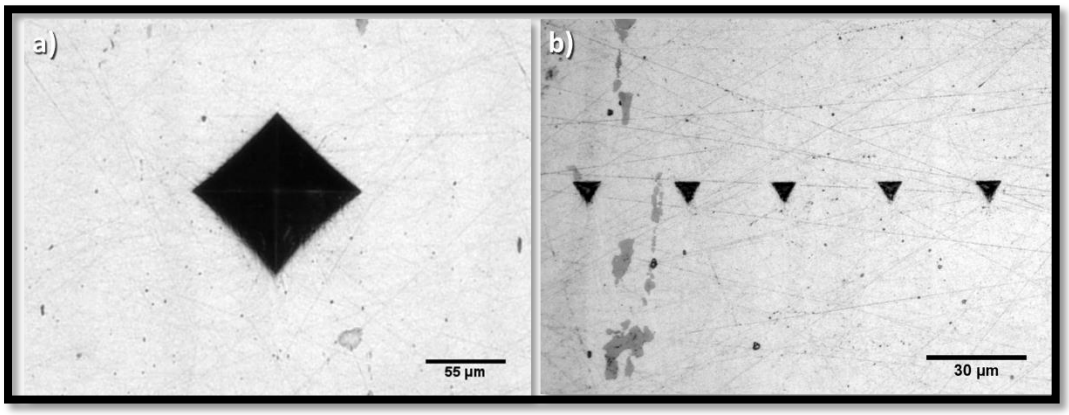

Figure 3-3. a) Micro-indentations; b) Nano-indentations.

3.1.2 Coatings

The Table 3-2 shows the characteristic features of the deposited coatings, thickness and porosity. The greater value of porosity, observed in the AT-13 (140) coating, may have been a consequence of the spreading of the powders during the thermal spraying process, which in turn was due to the greater distance between the gun

and the substrate, 140 mm; the same phenomenon was responsible for the higher thickness of this coating. The spreading of the molten particles depends on the temperature and speed at the impact with the substrate, as well the cooling kinetics of the substrate. Figure 3-4 and Figure 3-5 show the structure of the AT-13 coatings and their surface morphology.

Table 3-2. Thickness and porosity of the thermally sprayed layers.

	Substrates	BC	AT-13 (110)	AT-13 (140)
Thickness (µm)	3.95±0.02	164.39±16.36	124.23±18.65	141.07±23.27
Porosity (%)	-	18.2±1.4	14.81±3.16	24.51±3.66

The SEM observations of the coatings, deposited by oxyacetylene flame, showed a denser microstructure for the coating that was deposited at a shorter distance, 110 mm, this result is evidenced by the lower porosity level obtained in the AT-13 (110) coating. Both coatings, AT-13 (110) and AT-13 (140), exhibited a complex microstructure of several phases with the presence of porosity and unmelted particles. The microstructure of both coatings is constituted by splats/lamellae and globular pores and had not macro-cracks since the stresses produced during the formation of these multilayers were not enough to produce it, even though the splats formed after the quenching of the deposits had some micro-cracking as it is shown in Figure 3-5. This micro-cracking was observed in both coatings i.e., coatings sprayed at 110 and 140 mm standoff distances. The porosity of the top coat was measured by digital image analysis and determined according to the ASTM E2109. The porosity depends on the melting point of the powders, that is to say, if the flame does not reach the needed temperature to melt the ceramic particles they will not be melted efficiently, and consequently, the splats will not be formed adequately over unmelted particles, and this fact also explains the higher thickness in the AT-13 (140). In the absence of temperature and particle velocity measurements, it is assumed that the porous structure resulted from the low temperature, high cooling rates and low velocity of the sprayed particles, being this more noticeable at the greater standoff distance, 140 mm.

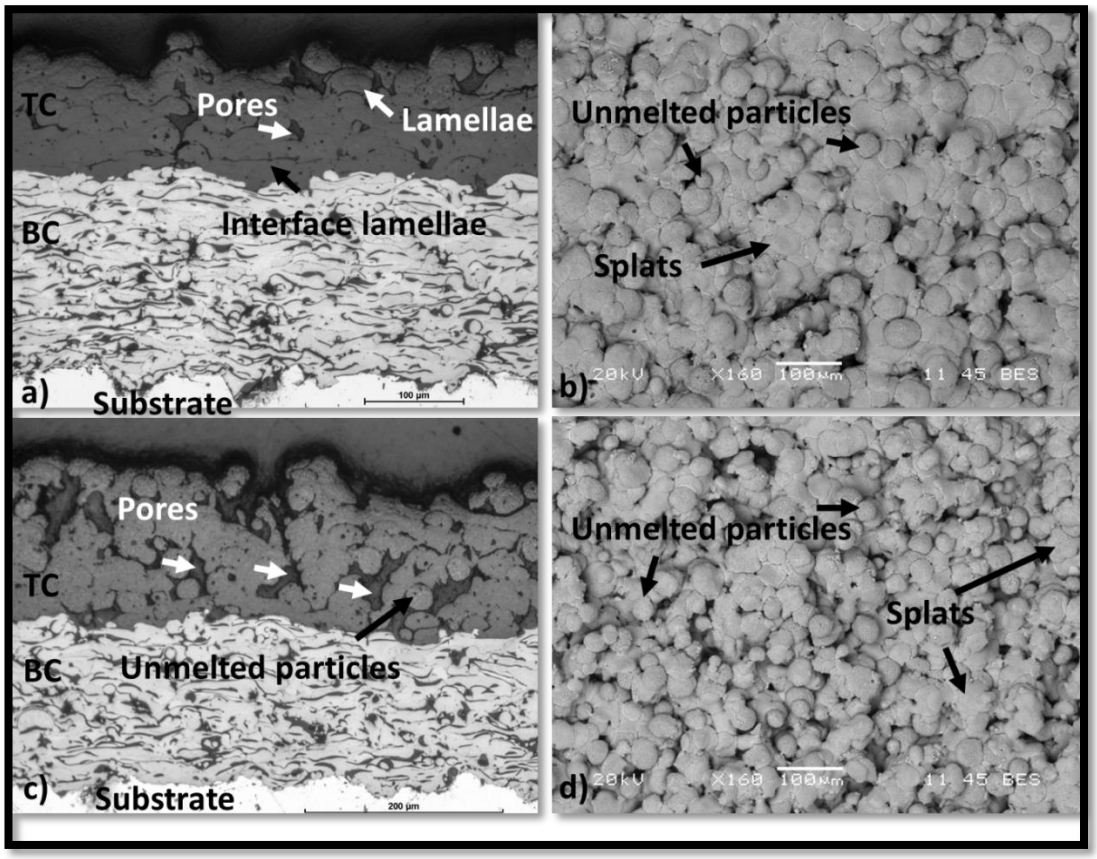

Figure 3-4. AT-13 coating systems. a) and b) structure and surface morphology of the AT-13 (110); c) and d) structure and surface morphology of the AT-13 (140).

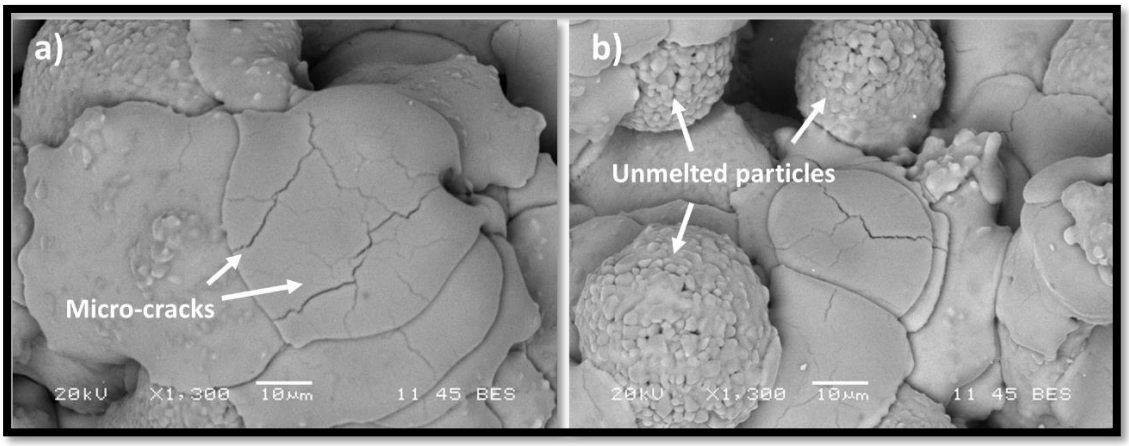

Figure 3-5. Splat morphology. a) AT-13 (110); b) AT-13 (140).

The roughness of the coatings was analyzed by using the mean roughness, Ra, as a qualitative measurement; values reported in Table 3-3, suggest that the BC was

deposited satisfactorily over the substrate (as seen in Figure 3-4), i.e., the Ra values of Substrate and BC were close enough; on the other hand, the AT-13 (110 and 140) coatings registered values 173.2 and 160.4% higher than the BC suggesting that the coatings exhibited poor particle melting during the spraying process.

Table 3-3. Roughness of the samples.

Layer	**Roughness** Ra (µm)
Substrate	6.71±0.69
Bond Coat	7.55±0.66
AT-13 (110) TC	18.33±1.48
AT-13 (140) TC	17.47±0.72

The results of the XRD for the AT-13 powders (Figure 3-6 a), exhibited typical peaks of α-alumina phase, titania, and Al_2TiO_5. After thermal spraying, it is observed that the largest difference between both coatings was due to the spraying distance which rendered a notable change in the content of the aluminum titanate (Al_2TiO_5), which was higher for the AT-13 (110). After the spraying process, the α-alumina phase suffered a partial transformation to γ-alumina as a consequence temperature conditions; these observations were in agreement with those reported in literature [68].

The alumina-titania systems have high tendency to produce different phases and crystallographic structure changes according to the cooling process, deposition techniques, material's spraying conditions, proportion of each component, and the characteristics of the coupling layer used; these last also affect the mechanical properties of the coatings, as well as the quantity and size of structural defects present in the coatings do [69], [70].

The presence of oxides in the TC generally results in an increase of its hardness that can also cause embrittlement because the oxidized splats are generally poorly linked with other splats/lamellae; Table 3-4 shows a summary of the phases that

were found in the powders and the deposited top coatings; the percentage of phases was estimated using the Rietveld method.

Table 3-4. Summary of phases found in the powders and the sprayed coatings.

Sample/Phase (%)	α-Al_2O_3	γ-Al_2O_3	TiO_2	Al_2TiO_5	Error
AT-13 powders	74.0	-	4.0	22.0	6.82
AT-13 (110) TC	72.7	15.0	-	12.3	6.69
AT-13 (140) TC	73.2	23.4	-	3.4	8.13

The hardness of the AT-13 top coatings is presented in Table 3-5; it is observed that hardness was higher for the denser coating, AT-13 (110); on the other hand, this coating has the highest amount of titanates, Al_2TiO_5; the greater the density of the coating, the greater the hardness. The scatteredness of the hardness values results from the differences in particles temperatures and velocities obtained during the deposition process, the microstructural defects, and the different phases present in the samples.

Table 3-5. Hv hardness of the top coatings, measured at the cross-section.

Coating system	Hardness (Hv)	Young's Modulus (GPa)
AT-13 (110)	1008.84±182.76	166.89±18.23
AT-13 (140)	844.00±249.38	136.11±28.32

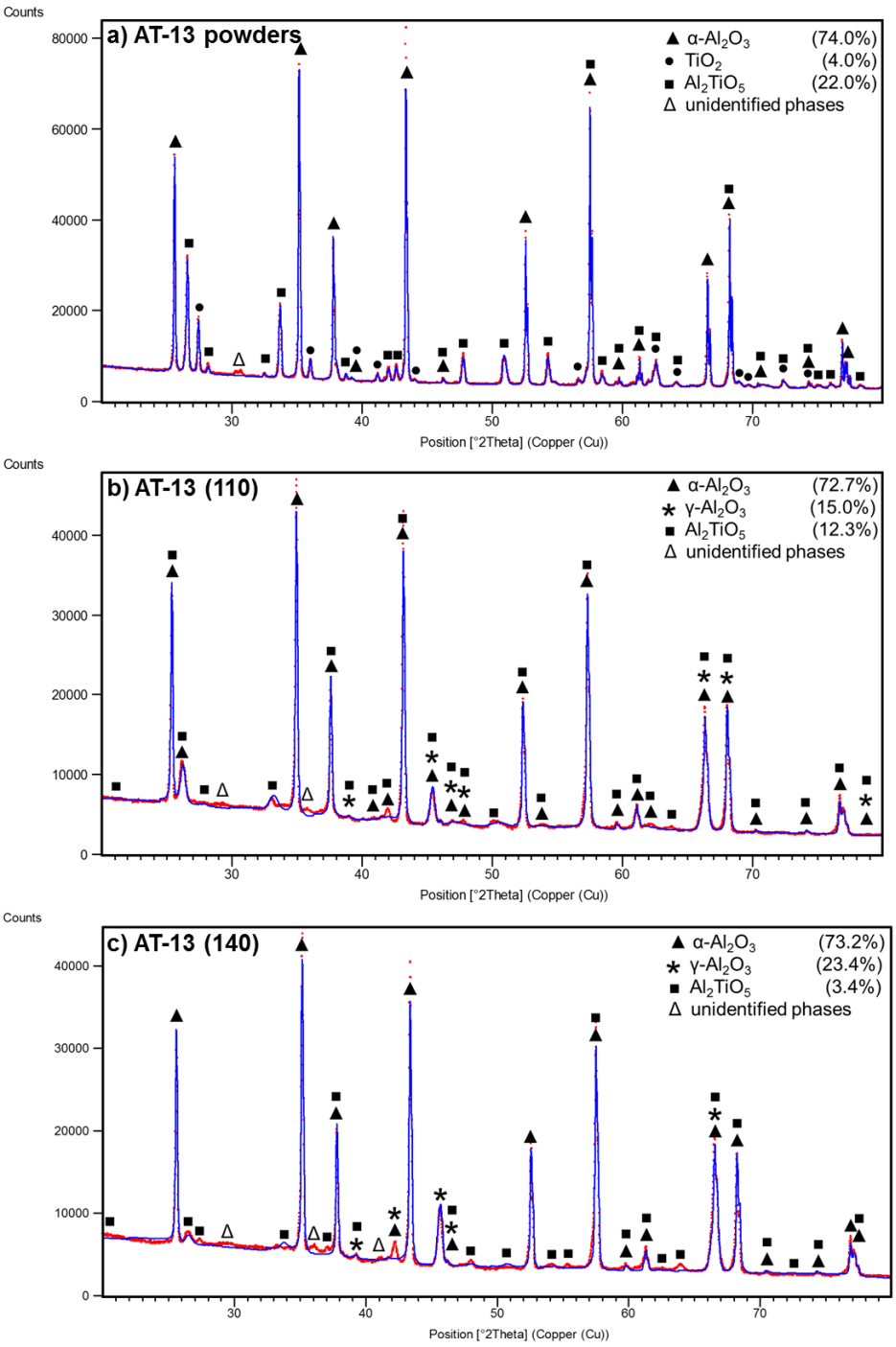

Figure 3-6. Diffractograms refined by the Rietveld method: a) AT-13 powders, b) AT-13 (110), and c) AT-13 (140).

The values of the Young's modulus for both AT-13 coatings experienced the same effect, where porosity played an important role; according to the literature, higher amounts of Al_2TiO_5 should diminish the values of E [69], but in this case, the lower porosity of the AT-13 (110) with respect to the AT-13 (140) was the cause; from another point of view, the relatively high porosity and imperfect contact between splats of the AT-13 (140) coatings was the consequence of the lower hardness and lower Young's modulus.

The diffractograms of the BC powders and the sprayed BC are shown in (Figure 3-7). It is observed a peak broadening due micro-strains introduced into the material during the thermal spraying process. As well, it is observed the transformation of the AlNi phase to Ni as consequence of the thermal process. Table 3-6 summarizes the phases found in the BC coatings and the BC as sprayed.

Table 3-6. Summary of phases found in the powders and the sprayed BC.

Sample/Phase (%)	Ni rich	Cr rich	AlNi	Error
BC powders	44.2	28.4	27.5	9.98
BC as sprayed	99.7	0	0.3	6.54

The values of the Young's modulus and the hardness of the bond coat are shown in Table 3-7. No appreciable changes were found.

Table 3-7. Hv hardness of the bond coat after thermally spraying the AT-13 top coats.

Bond coat	Hardness (Hv)	Young's Modulus (GPa)
From AT-13 (110)	328.53±35.02	153.30±15.20
From AT-13 (140)	326.21±27.24	149.95±6.61

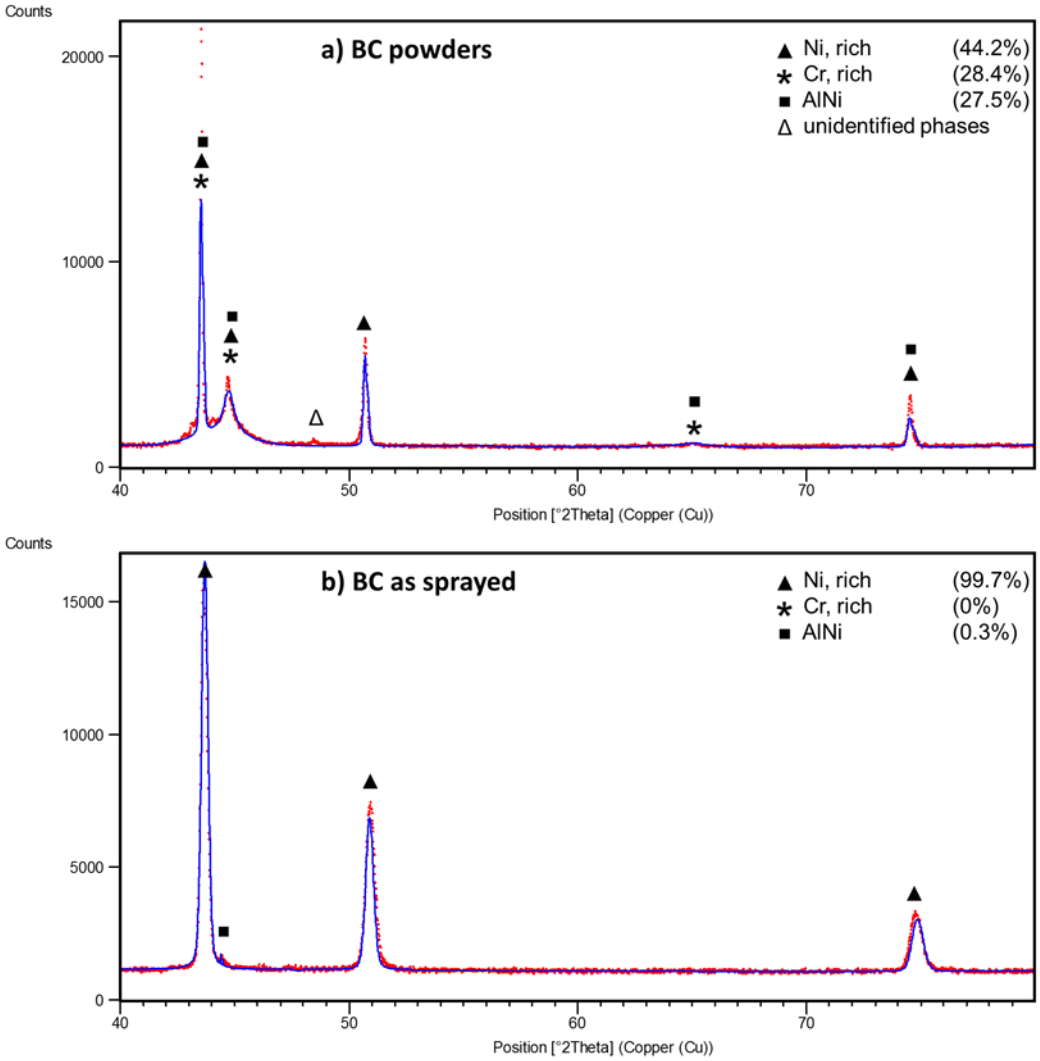

Figure 3-7. Diffractograms refined by the Rietveld method: a) BC powders, b) BC as sprayed.

3.2 Tensile tests

3.2.1 Substrates

The stress-strain curves at room and elevated temperature, for the AA7075-T6 bulk material and the coating systems {AT-13 (110) and AT-13 (140)}, are shown in Figure 3-8. Table 3-9 shows a summary of the main features extracted from the tensile test curves, and Table 3-8 shows the distribution of temperatures during the

tensile tests at elevated temperature; the temperature gradients shown in Table 3-8 were caused by the fact that the substrate material, AA7075, exhibits a high value of thermal conductivity; bear in mind that the substrates were in contact with the "cold grips" of the tensile testing machine during the runs.

From Table 3-8 it is also concluded that both coatings, AT-13 (110) and AT-13 (140), already gave an additional thermal protection to the substrate; due to the high values of thermal conductivity offered by the substrate, the Young's modulus, at elevated temperature, must calculated with the average temperature at which samples were held in this investigation (see Table 3-9 and Table 3-8). From Table 3-9 it is seen that the Young's Modulus of all the substrates experienced a reduction of about 26% during the tensile test at elevated temperature, as expected.

Table 3-8. Distribution of temperatures during the tensile tests, at elevated temperature; holding time 15 minutes. T1 was measured on the heated surface while T2 was measured onto the opposite surface.

SAMPLE	T1 (°C)	T2 (°C)	T-Average	ΔT
Substrate	260	126.7±16.7	193.3±8.3	133.3±16.7
AT-13 (110) system	260	143.3±27.2	201.7±13.6	116.7±27.2
AT-13 (140) system	260	158.7±34.4	209.3±17.2	101.3±34.4

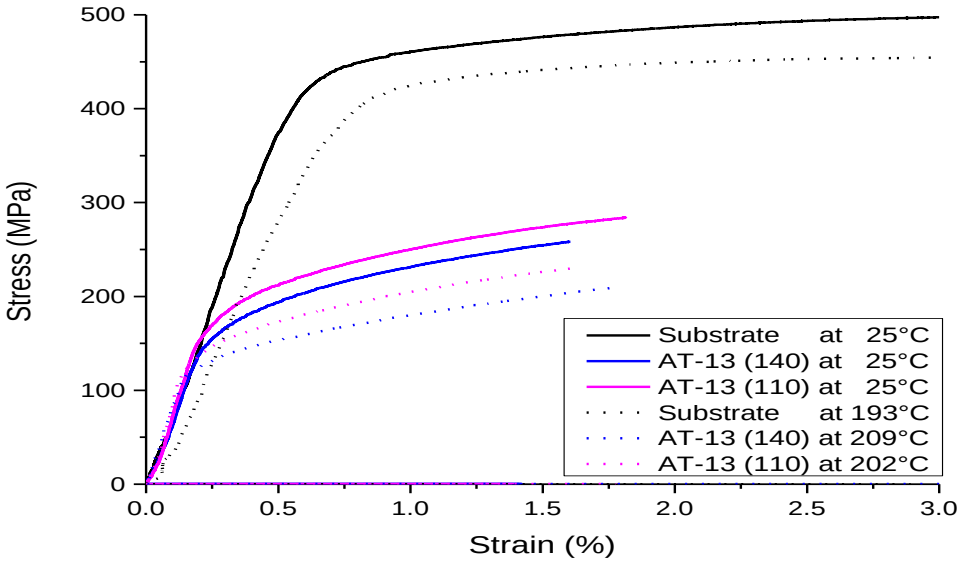

Figure 3-8. Stress-strain curves for uncoated and coated substrates.

Table 3-9. Young's modulus of AA7075 substrates, in their as received and thermally sprayed conditions, extracted from the stress-strain curves and nanoindentation.

	AA7075 Young's Moduli (GPa)		
Specimen	Room temperature (Tensile test)	Elevated temperature (Tensile test)	Room temperature (Nanoindentation)
AA7075-T6	78.97±1.24	61.79±2.66	82.16±2.58
AT-13 (110)	83.47±5.20	60.50±2.57	80.72±3.60
AT-13 (140)	82.80±8.06	58.90±12.91	79.73±2.68

3.2.2 Coating crack evolution (at room temperature)

The stress-strain curves shown in Figure 3-9 illustrates the cracking stages (or crack evolution), obtained in situ, for both AT-13 coating systems at room temperature; such cracking stages correspond to specific strain values which are summarized in Table 3-10; they consist of four stages **A, B, C,** and **D** that were observed with a high resolution video camera.

As the strain increases, the points **A, B, C,** and **D** manifest. It should be taken into account that most of the load is born by the substrate. The first transversal crack appears, at a critical strain, where the highest strain concentration is located in the coating, normal to the TC/BC interface; this critical strain corresponds to the first stage of cracking (A), beyond this point, other vertical cracks successively appear under the increasing tensile load, then, vertical cracks come to saturation. The effect of shear stress induced by the substrate deformation on the coating gradually vanishes because all interface delamination comes to a saturation state.

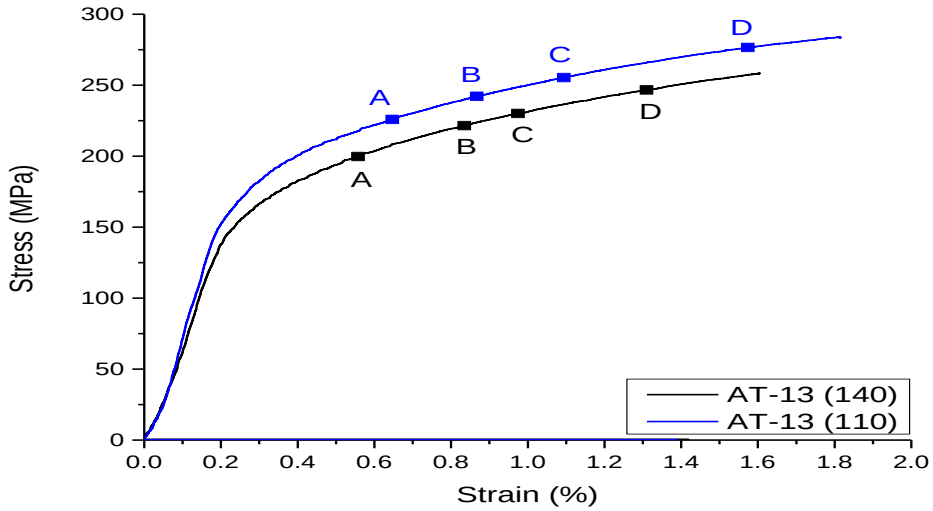

Figure 3-9. Stress-strain curves for the AT-13 (110 and 140) coatings showing the cracking stages.

The main stages observed during the tensile test are described as follows:

A. Crack initiation: The appearance of initial cracks is evidenced by changes in the coating surface, even though they are not completely visible; these cracks appear above a critical strain and then propagate throughout the coating.
B. Nucleation: The increase of the strain up to a value which is greater than the critical strain results in a rapid increase of the number of cracks, increasing the crack density in this fashion.

C. Propagation: At strains beyond A) and B), the increase in the transverse crack density slows down until it reaches a saturation point; until this point, transverse cracks had grown, now propagation stops.
D. Saturation point: Beyond this point, film decohesion, buckling, spallation, or delamination may occur for strips located between two successive transverse cracks, as the final stage.

Table 3-10. Cracking stages for AT-13 coatings at room temperature, in situ measured.

	Strain values (%)			
Coating system/Cracking stages	**A**	**B**	**C**	**D**
AT-13 (110)	0.70±0.08	1.00±0.09	1.21±0.11	1.77±0.19
AT-13 (140)	0.51±0.05	0.78±0.10	0.90±0.14	1.19±0.12

The Figure 3-10 shows the in situ observations of the cracking stages for the AT-13 (110) and AT-13 (140) coatings during room temperature tensile tests. The actual values obtained for the cracking stages A, B, C, and D, are summarized in Table 3-10. These values are in agreement with those reported by Zhou, M., et al. and Eberl, C. et al. whose reports rendered values between 0.35 and 0.50% for the critical strain (stage A) in ceramic coating systems [50], [51]; It should be born in mind that the spraying processes used by them, APS and EB-PVD, have higher energies for the deposition, i.e., higher temperatures and particle velocities, being enough to melt the ceramic particles and produce denser coatings.

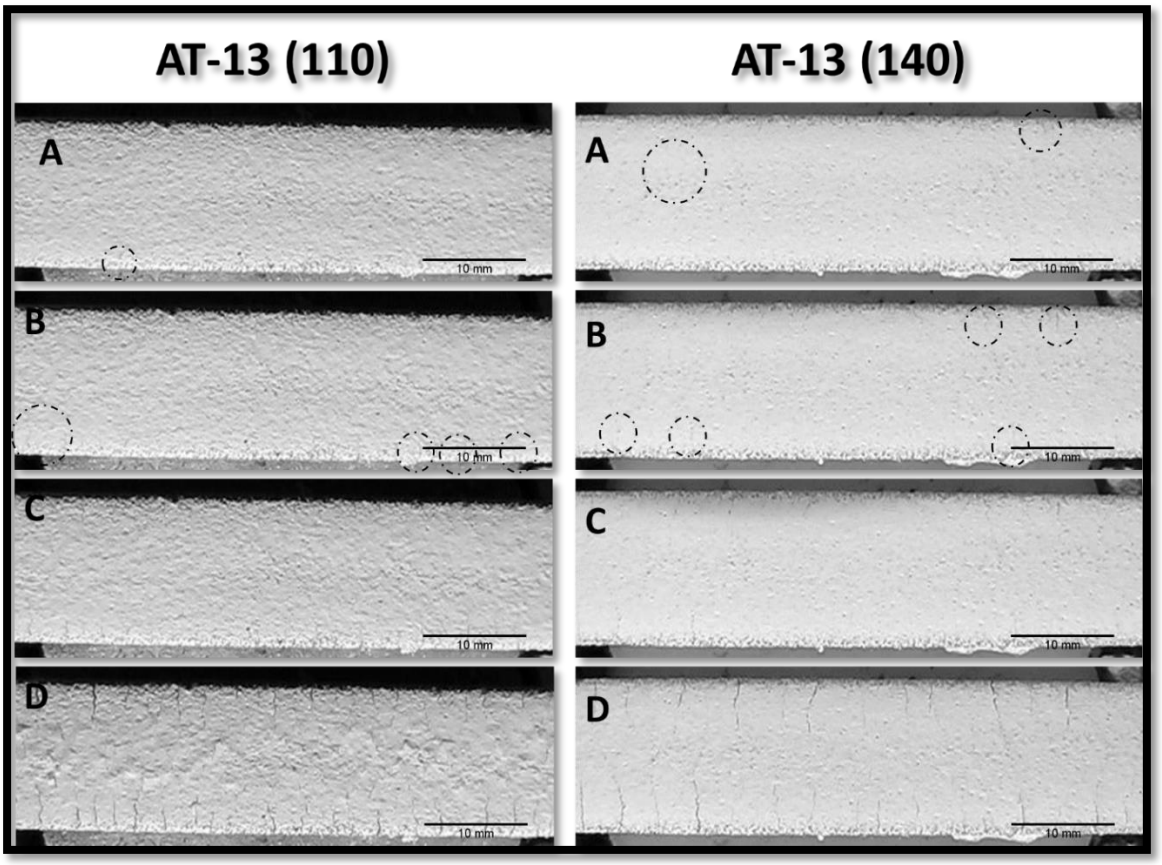

Figure 3-10. In situ observation of cracking stages during the tensile tests at room temperature.

It is observed that both coatings, AT-13 (110) and AT-13 (140), exhibited a similar behavior (at the surface) during the tensile test at room temperature; the main difference between them is the crack density beyond stage C, it was higher for the AT-13 (110) with a value of 0.7 cracks/mm; the AT-13 (140) had a value of about 0.44 cracks/mm meaning that the shear stresses are better transmitted to the AT-13 (110) coated system, i.e., the AT-13 (140) is more prone to delamination. This will be corroborated by metallographic cross sections in next chapter. Appendix D, includes the panoramic micrographs of stage C.

3.2.3 Coating crack evolution (after high temperature tensile test)

In order to have a good comparison of the failure at room temperature and elevated temperature during the tensile tests, the AT-13 (110) and AT-13 (140) coatings were loaded up to the strain corresponding to the cracking stage **C** which was previously observed in situ where the measurement of the crack density is easily accomplished.

Figure 3-11 shows the cross-sectional micrographs of the coatings AT-13 (110) and AT-13 (140) at the cracking stage **C** where the respective strains are 1.21±0.11% and 0.90±0.14%, according to the in situ measurements at room temperature. At this stage, it is observed that the cracks in the BC have increased their number i.e., the crack density; most of the cracks have passed through the BC which confirms that the failure initiates at the bond coating. This behavior is promoted due to the great difference in the Young's moduli (measured by nanoindentation) of the AA7075 substrates and BC coatings, ~80 and ~150 GPa respectively, which reveals that the strain compatibility between them is poor. On the other hand, it is important to note that the value of the Young's modulus for the BC is much closer to the AT-13 coatings {AT-13 (110), ~170 GPa; AT-13 (140), ~140 GPa} than that of the substrates, which means that the strain compatibility between BC and TC is better than between BC and substrate.

Table 3-11 summarizes the different values of crack density obtained either at room temperature and elevated temperature for both coatings. It is worth mentioning, that the crack density values, after elevated temperature tests (obtained ex situ), were focused on the vertical cracking observed in the BC, and they do not differ that much from those obtained during the in situ observation, which have lower resolution.

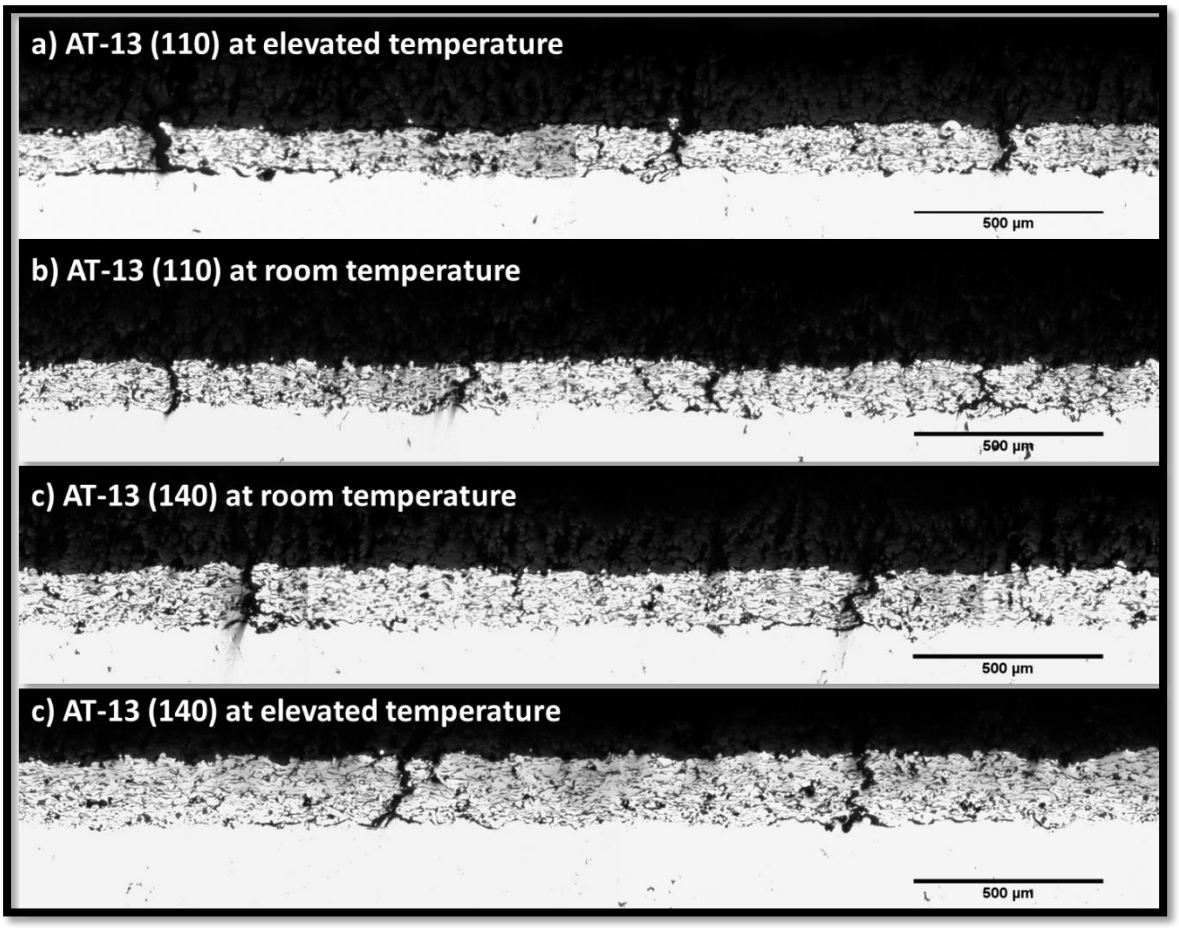

Figure 3-11. Ex situ observations of cracking stage “C” for both coatings after room and elevated temperature testing. Vacuum impregnated samples.

Table 3-11. Comparison of in situ and ex situ measures for crack density (cracks/mm) at stage C.

Temperature	**Coating**	**In situ**	**Ex situ**
Room temperature	AT-13 (110)	0.70	1.03
Elevated temperature		N/A	0.91
Room temperature	AT-13 (140)	0.44	0.56
Elevated temperature		N/A	0.58

A comparison between both coatings after the room temperature tensile testing shows that the crack density, measured in situ, of the AT-13 (140) is 37.14% smaller than that of the AT-13 (110); a similar value was obtained in the ex situ measurement, 56.4% for the same coating. At elevated temperature, the ex situ observation showed that the drop of the crack density is still having a similar trend, 63% for the AT-13 (140). These results reveal that the crack density, cracking in general, depends on the deformation of the substrate in first instance: Note that in Appendix D, in regions near to the clamps (low deformation: trough transversal cracks) the crack patterns differ from that on the middle of the sample (high deformation: delamination plus trough transversal cracks). On the other hand, the intrinsic characteristics of a thermally sprayed coating, such as porosity, and the level of bonding between splats and/or unmelted particles, play an important role on how the interface stress (during tensile test) is distributed. The strength of a porous material depends on pore distribution, pore morphology, and pore size, with high porosity generally leading to lower strength [71], [72]. Then, the intrinsic characteristics of the coating also control the way cracks initiate and propagate. Note for example that the BC/substrate interface has small cracks in the AT-13 (110) system than in the AT-13 (140) one, in other words the interface fracture toughness is bigger for AT 13 (110) which produces a good load transmission and therefore a bigger crack density.

These results for crack density are in agreement with the work carried out by [73], where three different TBC coatings (in terms fracture strength) were evaluated (see Figure 3-12).

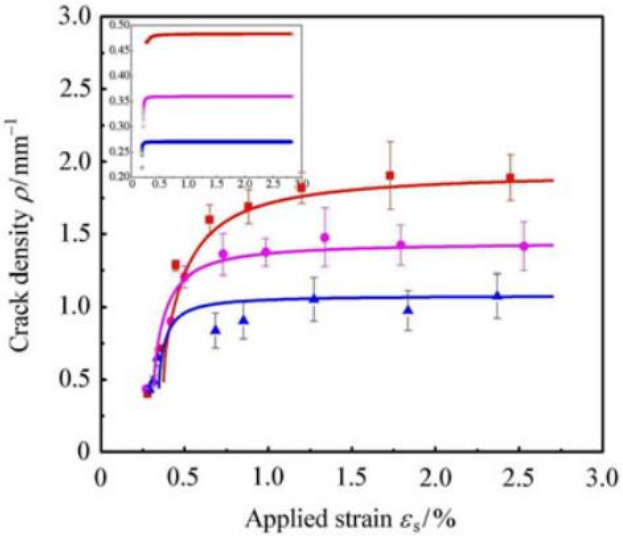

Figure 3-12. Crack density during tensile tests of TBCs. Higher fracture strength (red line), middle (magenta line), lower (blue line) [73].

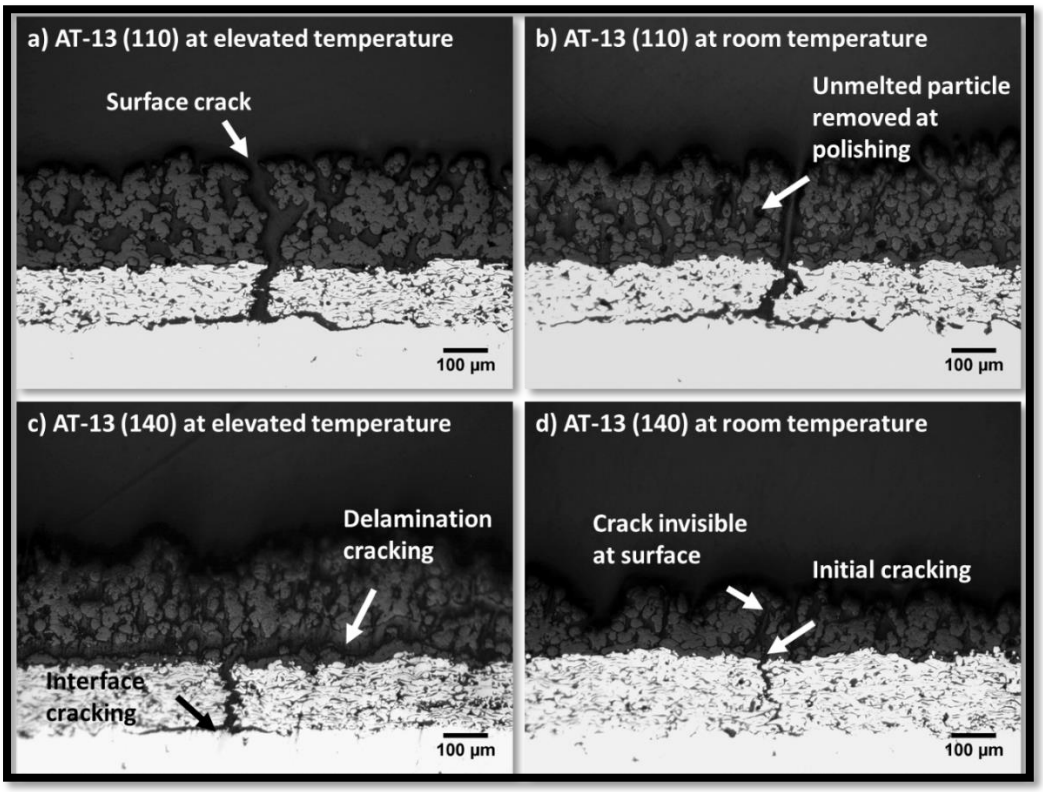

Figure 3-13. Crack morphology for both coatings after room and elevated temperature tensile testing. a) and b) AT-13 (110); c) and d) AT-13 (140).

Figure 3-13 shows a close-up of the features of cracking that were observed in both coatings. It is seen that the cracks travelled between lamellae due to the poor bonding of the splats after the spraying process as discussed earlier. In Figure 3-13 a, is seen that the initial cracking started at the BC/Substrate interface where the higher shear stress is located. The coating AT-13 (140), the one with the higher porosity, which suffered the poorest bonding of the coating due to the great number of unmelted particles and porosity, showed smaller crack density values since it had some delamination cracking that appeared upon the TC/BC interface and some cracks did not show up at the surface in spite of their extent; this is attributed to the inadequate transmission of the shear stress at the interface [45], [41].

The micrographs shown in Figure 3-11 and Figure 3-13 revealed that the place where the coating, when submitted to tension at room or high temperature, was susceptible to spallation, it was mainly in the BC/substrate interface which confirms that the BC does not exhibit strain compatibility compared to that of the substrate. However, elevated temperature promoted delamination cracking between BC and TC, particularly for the AT-13 (140) system, which is confirmed by the drop in the crack density at elevated temperature; again, it is an effect of the shear stress that was diminished as consequence of the temperature.

3.2.4 Weibull statistics

Weibull statistics was used to estimate the mechanical behavior of the coatings through the cracking stages A, B, C, and D. The Weibull plots (Figure 3-14 b and c) show that, in general terms, despite of the differences found in both coatings, the cracking stages for the AT-13 (110) and the AT-13 (140) exhibit a similar behavior.

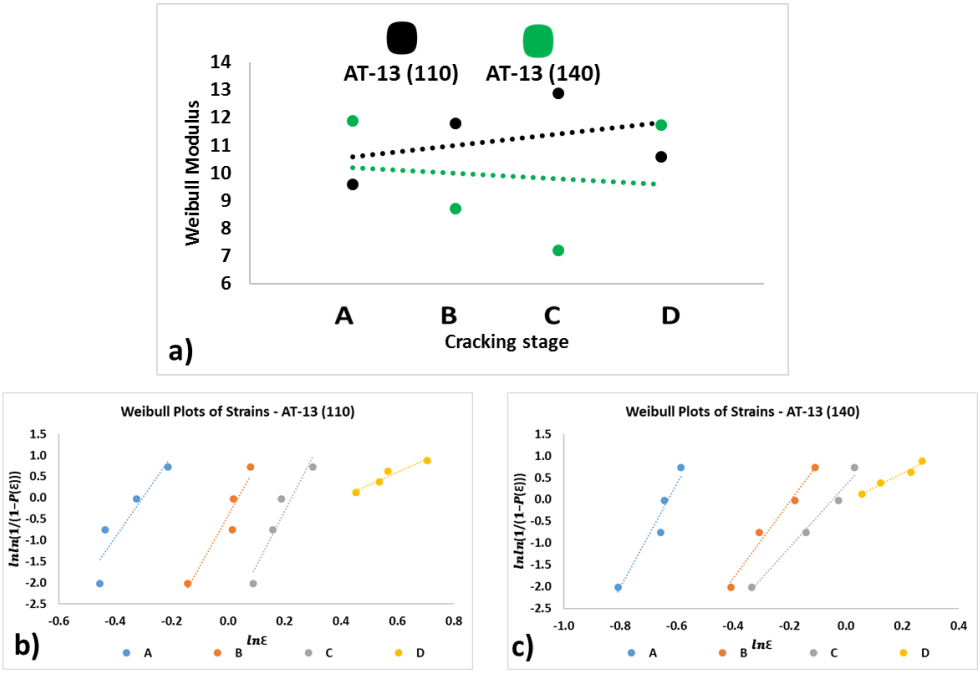

Figure 3-14. a) Weibull moduli of the cracking stages, A, B, C, and D; b) and c) Weibull plots of both coatings.

For having a better glance of their performance, the Weibull moduli was used (Figure 3-14 a). Weibull modulus gives a direct indication of the scatteredness, the higher the Weibull modulus, the more consistent the values for the cracking stages, i.e., the higher the Weibull modulus, the lower the standard deviation and the scatteredness of the data with respect to the average value. Table 3-12 presents a summary of the values obtained from the tensile tests (strain and stress) along with the Weibull moduli for both coating systems.

Table 3-12. Weibull moduli summary of the cracking stages A, B, C, and D, for the At-13 (110) and AT-13 (140) coatings.

CRACKING STAGE	AT-13 (110) COATING SYSTEM		
	Weibull moduli	Strain (%)	Stress (MPa)
A	9.59	0.70±0.08	224.47±20.16
B	11.78	1.00±0.09	245.14±15.33
C	12.87	1.21±0.11	256.83±16.65
D	10.58	1.77±0.19	280.01±13.92

CRACKING STAGE	AT-13 (140) COATING SYSTEM		
	Weibull moduli	Strain (%)	Stress (MPa)
A	11.88	0.51±0.05	190.38±13.25
B	8.73	0.78±0.10	212.53±18.82
C	7.21	0.90±0.14	219.96±20.40
D	11.72	1.19±0.12	236.21±17.93

A quick view of the measured Weibull moduli for both coatings, may give a wrong interpretation of the results, but this is explained as follows:

At cracking stage A (crack nucleation), the Weibull modulus of the AT-13 (140) suggests lower scatteredness, compared to its counterpart; in this coating the obtention of the strain values had lower scatter because it exhibited the lower bonding between unmelted particles and splats, favoring the spreading of the cracks, also, the shear stress that was transferred from the substrate to the overlaying layers is better distributed in the AT-13 (110); this last coating, AT-13 (110), is capable of withstanding further strain and higher loads than those born by the AT-13 (140), where shear is not well distributed, having regions with higher concentration of shear stress which will fail the first. It should be taken into account that at this stage, the shear stress is still being homogenized and the cracks are growing (or nucleating) i.e., they are not completely visible at the surface, which makes it difficult to perform an accurate reading from the in situ video.

On the other hand, it is seen that both coatings have an opposite trend for the cracking stages B, and C; the scatteredness of the data decreases for the AT-13 (110) and increases for the AT-13 (140) as a general trend. At cracking stage B (crack multiplication), once the shear stress has been transferred homogeneously to the denser coating AT-13 (110), the crack multiplication is easier to follow, but in the coating AT-13 (140), as the shear stress transfer was not optimum from a start, A, it affects notoriously the following stages.

Finally, at stage D, the Weibull modulus is bigger for the AT-(140), but the values for strain must not be considered for the evaluation, because from stage D (crack saturation), the observations are more susceptible to subjective measurement (the

shear stresses have been distributed between the individual segments, far beyond, the only change that will be observed is the increase of the cracks' spacing. At this stage, the spalling also makes the readings more difficult, i.e., not reliable.

On the other hand, the intrinsic characteristics of a thermally sprayed coating, such as porosity, and the level of bonding between splats and/or unmelted particles, play an important role on how the interface stress (during tensile test) is homogeneously distributed at the interfaces; the surface crack density depends on the fracture strength of the ceramic coating, the shear strength of the interface and the residual strain in the ceramic coating. It is concluded that the cracking stages may be used to evaluate the adhesion strength of the coatings, at least, as a comparison between batches of coatings.

At elevated temperatures, as shown in Figure 3-11, both coatings were susceptible to delamination cracking which in turn is caused by a loss of transfer of the shear stress at the interface; this is confirmed by the diminution in the crack density values at elevated temperature (see Table 3-11).

In general terms the coating system AT-13 (110), when compared to the AT-13 (140), had a better bonding to the substrate, and a higher fracture strength this confirmed by the values of crack density; this coating system may be a good candidate for protecting abradable components. On the other hand, the coating system AT-13 (140) may be a good candidate for high temperature protection of static components, given its elevated porosity that could offer additional thermal protection, though, it has the lower fracture strength.

4 Conclusions and recommendations

4.1 Conclusions

The thermal spraying process affected considerably the mechanical properties of the AA7075 substrates as a consequence of the heat treatment caused during the exposition to the thermic conditions that produced an overaging of the base metal.

The greater value of porosity observed in the AT-13 (140) coating may have been a consequence of the spreading of the powders during the thermal spraying process, which in turn was due to the greater distance between the gun and the substrate. The same phenomenon was responsible for the higher values measured in the thickness in this coating (bigger porosity). Also, the flame did not reach the needed temperature to melt the ceramic particles which rendered coatings with high values of porosity, affecting also the thickness of the coatings.

The parameters used for the deposition of the AT-13 coatings onto AA7075 substrates were not efficient due to the formation of microcracks in the splats/lamellae, and the high values of porosity that were achieved.

The methodology presented herein, showed to be accurate enough for measuring critical strains in coating systems, and rendered a good result showing that the adhesion of the coating may be influenced be the spraying distance, and evaluated by crack density.

Both coatings provided thermal insulation to the substrates, being the coating with the highest porosity the one with the better performance in terms of thermal

insulation, but at elevated temperatures, both coatings were susceptible to delamination cracking which in turn is caused by the loss of shear stress transfer from the substrate to the coating system; this was confirmed by the diminution in the crack density values at elevated temperature.

In general terms the coating system AT-13 (110), when compared to the AT-13 (140), had a better bonding to the substrate, and a higher fracture strength, this confirmed by the values of crack density.

The AT-13 (110) coating system may be a good candidate for protecting abradable components. On the other hand, the coating system AT-13 (140) may be a good candidate for high temperature protection, given its elevated porosity that could offer additional thermal protection, though, it has the lower fracture strength which is a bad characteristic for demanding applications.

The bond coat used in this study showed a poor strain compatibility with the substrate due to the differences in the Young's modulus; this behavior was the main cause of failure of the coatings.

The intrinsic characteristics of a thermally sprayed coating, such as porosity, and the level of bonding between splats and/or unmelted particles, play an important role on how the interface stress is transferred; the surface crack density depends on the fracture strength of the ceramic coating and the adhesion between layers.

4.2 Recommendations

The improvement of methods for measuring, in situ, the real behavior of ceramic coatings may be developed by the introduction of different techniques such as acoustic emission, and better image acquisition equipment and techniques, e.g., digital image correlation, and acoustic emission.

The implementation of hot grips, for the tensile testing at high temperatures will reduce considerably the error that is caused by the thermal transfer between the hot samples and the “cold grips”.

Study performance of the AT-13 coatings proposed in here when deposited onto different substrates, with different thermal conductivities, as well as evaluating a wide range of spraying standoff distances.

Study the compatibility between the BC and the AA7075 substrates, and/or thermal treatments that may ensure the strain compatibility between them.

Study the effect of the porosity in the thermal isolation and mechanical properties during tensile tests at high temperatures.

A. Appendix: Tensile test machine

A re-design of a classical Monsanto tensometer was performed in order to be able of carrying out tensile tests at high temperatures.

The poster titled “CLAMPS MATERIAL SELECTION FOR A HOUNSFIELD TENSILE TEST MACHINE: REDESIGN FOR HIGH TEMPERATURE TENSILE TEST CONDITIONS” was presented at the VIII Congreso Internacional de Materiales - CIM 2015 that was held at Paipa - Boyacá – Colombia, October 28 – 30, 2015.

Abstract: Currently, many materials are required to operate at high temperatures so that the knowledge of their mechanical properties at these temperatures is essential. This work shows the materials selection method for the clamps of a Hounsfield W-type tensile test machine that was adapted to perform tests at temperatures up to 1000°C. The structure of the machine including the source of heat was modelled using Ansys FE software in order to get the Von Mises stresses and temperature distributions in the clamps. A maximum temperature of 104°C at the maximum Misses stress zone of 1078 MPa was found. The Ashby’s method for materials selection was implemented defining as objective function, for a contact situation, to minimize the cost given a yield stress strength and as a constraint the maximum operating temperature and resistance to oxidation at 500°C. The selected material was an AISI 420 stainless steel quench and tempered at 204°C, which is reported as the recommended material in the literature for this application. This confirms that the Ashby’s method is a powerful tool for materials selection, particularly because of it is easy to implement, resulting in efficiency and cost reduction in the design of machines.

Keywords: Tensile test, high temperature, materials selection, clamps, Ashby's method.

This equipment is instrumented with a gauge unit capable to measure strains, with a resolution as low as 3 µm. To achieve the high-temperatures, the specimen is heated, with a MC-GAXP-309 spiral micro-heater, upon the coating surface and the temperature measurement is carried out with contact thermocouples k-type.

Figure 4-1. Original Monsanto Tensometer.

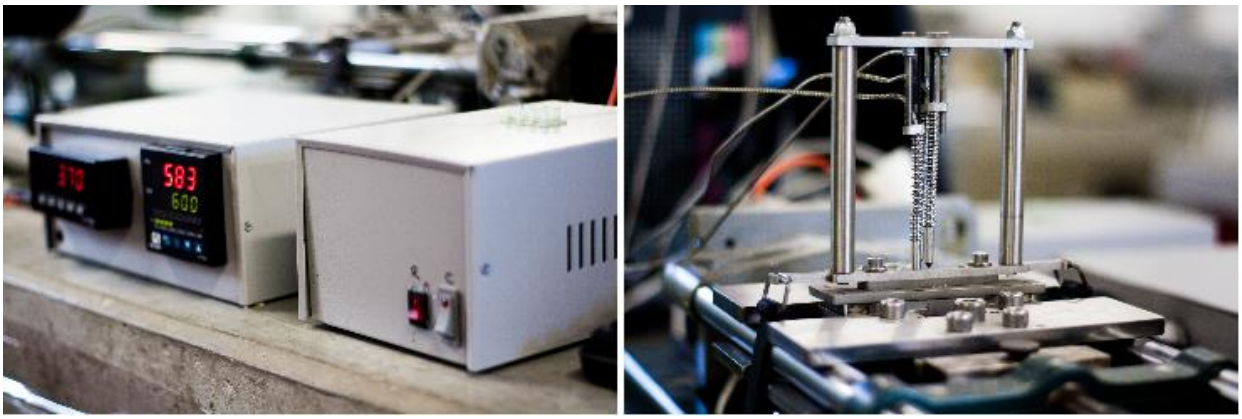

Figure 4-2. Monsanto tensometer modified for high temperature testing.

[9] The spyral microheater was bought at Micropyretics Heater International, Inc.

VIII CIM
CONGRESO INTERNACIONAL DE MATERIALES
2015

SELECCIÓN DEL MATERIAL PARA MORDAZAS DE UNA MÁQUINA DE TRACCIÓN HOUNSFIELD: ADAPTACIÓN PARA PRUEBAS DE TRACCIÓN A ALTA TEMPERATURA.

José David Acosta Correa[a] & Julián Mateo Ruiz Urrea[b] & Carlos Mario Serna[c] & Juan Manuel Meza Meza[d]

[a]Facultad de Minas, Universidad Nacional de Colombia, Medellín, Colombia. jodacostaco@unal.edu.co
[b]Facultad de Minas, Universidad Nacional de Colombia, Medellín, Colombia. jmruizu@unal.edu.co
[c]Facultad de Minas, Universidad Nacional de Colombia, Medellín, Colombia. cmsernaz@unal.edu.co
[d]Facultad de Minas, Universidad Nacional de Colombia, Medellín, Colombia. jmmezam@unal.edu.co

RESUMEN:

Muchos materiales se requieren para funcionar a altas temperaturas por lo que el conocimiento de sus propiedades mecánicas a dichas temperaturas es imprescindible. En este trabajo se muestra el método de selección del material para la mordaza de una máquina de tracción Hounsfield W-Type que fue adaptada para realizar pruebas de tracción a temperaturas de hasta 1000 °C. Se utilizó el programa ANSYS para modelar la estructura completa de la máquina, se incluyó la fuente de generación de calor y se determinó los esfuerzos de Von Mises y en las mordazas se encontró que la zona de mayor esfuerzo está sometida a una temperatura de 104 °C y a un esfuerzo principal de 1074 MPa. Para la selección del material se aplicó el método de Ashby definiendo como función objetivo, para una situación de contacto, minimizar el precio dada una resistencia a la fluencia y restringiendo la temperatura máxima de operación y buena resistencia a la oxidación a 500°C. El material seleccionado fue un acero inoxidable AISI 420 templado y revenido a 204°C, el cual es el material recomendado en la literatura para estas aplicaciones. Con esto se corrobora que el método de Ashby es una herramienta poderosa para la selección de materiales, particularmente por la facilidad de su implementación lo que redunda en la eficiencia y reducción de costos en los proyectos de diseño de máquinas.

INTRODUCCIÓN

El creciente interés acerca de estructuras y componentes resistentes a altas temperaturas en aplicaciones nucleares, en generación de energía eléctrica con turbinas a gas, la aeronáutica, el sector aeroespacial y el de autos de competición, ha llevado a la necesidad de medir las propiedades y analizar el desempeño de diferentes tipos de materiales a altas temperaturas, cuando su uso o aplicación se da directamente en estas condiciones de servicio. Para medir propiedades mecánicas a altas temperaturas se diseñó y adaptó a una máquina Hounsfield W-type un sistema de mordazas que soporta probetas dog bone por traba mecánica y un hogar para resistencias electricas. Este tipo de probetas recomendadas por la norma ASTM E8 y la norma ASTM C1366-04, cumplen con los requerimientos para hacer tracción en diferentes tipos de materiales.

SELECCIÓN DEL MATERIAL DE LAS MORDAZAS.

El método Ashby, es un método gráfico que establece un criterio y desarrolla un procedimiento sistemático para la selección de procesos y materiales.

Requerimiento de diseño	Índice
-Minimizar el precio, maximizando la rigidez	E/ρ*$
Minimizar el precio, maximizando la resistencia a la fluencia	σ_y/ρ*$

Traducción de requerimientos de diseño en índices.

Donde:
E: Módulo elástico
ρ: Densidad
$: Precio por kilogramo
σy: Límite de fluencia

La normas ASTM E21 y ASTM C6613, recomiendan para el sistema de sujeción una buena rigidez y resistencia a la fluencia en el material de este, evitando al máximo las deformaciones debidas a los esfuerzos mecánicos.

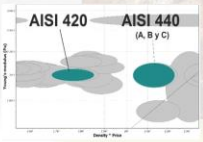

Gráfica E vs ρ*$.

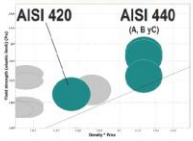

Gráfica σ_y vs ρ*$.

SIMULACIÓN

La modelación de la condiciones de servicio de las mordazas se realizó separando los fenómenos mecánicos de los térmicos, por medio de simulaciones diferentes.

Se modeló el proceso mecánico, con la condición de fuerzas más críticas (19600N) a temperatura ambiente, y el proceso térmico con la condición más critica a 1000°C en la resistencia eléctrica, sin aplicación de fuerzas en la mordaza

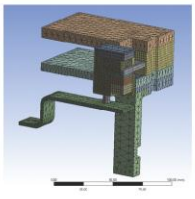

Simplificación del modelo mecánico evaluado por FEM.

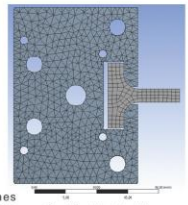

Simplificación del modelo térmico evaluado por FEM.

MALLADO

El mallado en las simulaciones se hizo con elementos tetraédricos, recomendados para las geometrías superficiales variables de los elementos tratados, los cuales, aseguran una calidad de elemento para la simulación alta (entre 0.7 y 0.9), según los estándares del software ANSYS 15.0.

RESULTADOS Y DISCUSIÓN.

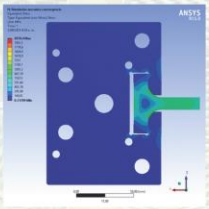

Esfuerzos mecánicos en el montaje probeta-mordaza con una fuerza de tracción de 19600N.

El punto de máxima solicitación en la mordaza se determinó a partir de las simulaciones mecánicas, éste se encontró en la superficie de la base de las vigas en voladizo de la mordaza, con un valor de esfuerzo que converge a 1073.7MPa, y en este punto, la simulación térmica arroja una temperatura de 104°C con un cambio de 0.283% y 0,463% respectivamente, entre las últimas dos simulaciones de cada uno de los modelos.

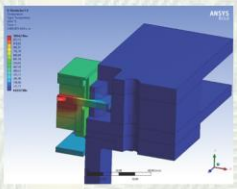

Distribución de temperaturas con resistencia a 1000°C en el sistema de mordazas.

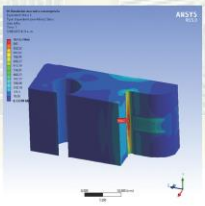

Sección de máximo esfuerzo mecánico en mordaza con ensayo de tensión de 19600N.

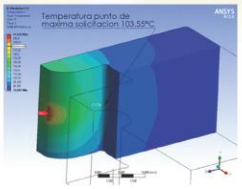

Sección de máxima temperatura y máxima temperatura en punto de máxima solicitación con resistencia eléctrica a 1000°C.

Se estableció una temperatura máxima en la mordaza de 213.62°C y un esfuerzo de alrededor de 300MPa en este punto, esfuerzo despreciable dada la condición. Por esta razón, los parámetros de selección de materiales se tomaron en el punto de máxima solicitación mecánica.

Las propiedades mecánicas del acero AISI 420 a una temperatura de 104 °C están por encima de las requeridas en el funcionamiento, lo cual muestra que la selección de este material es la más idónea para esta aplicación.

CONCLUSIÓN:

El método Ashby indica que el criterio para la selección del material de las mordazas con un criterio de bajo costo mostró que el mejor material para esta componente es el acero inoxidable martensítico AISI 420, cumpliendo con las restricciones de servicio que incluyen esfuerzos y temperatura.

Uptc Universidad Pedagógica y Tecnológica de Colombia
CIAD
INGENIERÍA
Incitema Instituto para la Investigación e Innovación en Ciencia y Tecnología de Materiales.

B. Appendix: Another works - Poster

The poster titled “MICROMECHANICAL BEHAVIOR OF THERMAL BARRIER COATINGS AFTER ISOTHERMAL OXIDATION” was presented in the Nanomechanical Testing in Materials Research and Development V that was held at Albufeira, Portugal, October 4 – 9, 2015.

Abstract: Thermal protection of metallic components by using ceramic coatings like thermal barrier coatings (TBCs) is widely used, in rocket engines, aircraft industry and gas turbines for power generation to reduce the substrate temperature up to 165°C. This technology diminishes the heat transfer in combustor, initial rotor blades and nozzles guide vanes, so that turbines have taken special advantage of these coatings to meet increasing demands for greater fuel efficiency, lower NOx emissions and higher power and thrust (Ciniviz, Canli, Kose, Salman, & Solmaz, 2012). Thermal barrier coatings, apart from thermal protection are also used to protect against abrasion, oxidation and corrosion (Evans & Hutchinson, 1995).

The understanding of the mechanical behavior of TBCs in both as-sprayed and thermal loading conditions is of great importance for the evaluation of components life. However, it is challenging to determine the true mechanical behavior because of the substantial differences, between each layer (TC, BC, and substrate), since the difficulty to prepare the sample´s surface and its high contents of pores, cracks and defects.

This work reports on the mechanical characterization of APS 6-8 wt.% yttria stabilized zirconia (YSZ) as top layer bonded by an HVOF NiCoCrAlY layer to a

superalloy substrate (Inconel 625) using the micro- and nano-indentation techniques on test specimens after being subjected to isothermal-oxidation at 1100°C and different time exposition (0, 200, 400, 600, 800, 1000, and 1700 hours).

Observations under optical and SEM microscopy were performed in order to study the variation of the mechanical properties such as hardness, young's modulus, and fracture toughness within the ceramic top layer after isothermal oxidation.

The hardness and Young's modulus of the ceramic layer showed an increase until 600h exposition which can be explained by sintering phenomenon. From 600h up to 1700h the Young's showed a stabilization due to the equilibrium of sintering and phase transformation mechanisms, but hardness continued its increasing rate.
The fracture toughness of the ceramic coating showed a softening condition of about 23% during the whole range of time for isothermal oxidation as a consequence of the detriment of the ceramic layer.

Results show that sintering phenomena, TGO growth and phase transformation give a complex state of stresses of the coating system which will have great influence on its performance during regime operation. It is concluded damage of the coating is proportional to the extent of time exposition.

Key Words: Thermal barrier coatings, fracture toughness, mechanical behavior, nanoindentation, thermal aging.

Micromechanical Behavior of TBCs After Isothermal Oxidation

Deiby Maya, Carlos Serna, Augusto Barrios, Pablo Gómez, Alejandro Toro, Juan Meza.
Tribology and Surfaces Group (GTS), Universidad Nacional de Colombia
Empresas Públicas de Medellín (EPM Group)

Abstract

Thermal protection of metallic components by Thermal Barrier Coatings, TBCs, is widely used in rocket engines, aircraft industry and gas turbines for power generation; this technology reduces substrates temperature up to 165°C. Apart from thermal protection they can also protect against abrasion, oxidation and corrosion.

This work reports on the mechanical characterization of APS 6-8 wt.% Yttria Stabilized Zirconia (YSZ) as top layer, bonded by an HVOF NiCoCrAlY layer to a superalloy substrate (Inconel 625), using micro- and nano-indentation techniques on test specimens after heat treatment at 1100°C and different exposure times (0, 200, 400, 600, 800, 1000, and 1700 hours).

The fracture toughness of the ceramic coating was measured trough IF method, in conjunction with failure statistics, proved to be a powerful tool that helps to understand microstructural and mechanical evolution of the coating due to high temperature exposition.

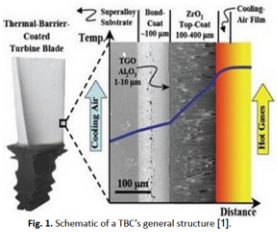

Fig. 1. Schematic of a TBC's general structure [1].

Materials and Methods

Test specimens, with dimensions of 1.7 x 1.7 cm, were heat treated at 1100°C during 0, 200, 400, 600, 800, 1000, and 1700 hours respectively, then they were mounted in phenolic resin, and samples were extracted for metallographic preparation: Grinding with sand paper Nº 400 and 600 (during 15 min); polishing with diamond suspension of 12, 6, 3 µm (during 15 min) and 1 µm (during 60 min), keeping a pressure of 37.5±3.54 KPa.

Nano- and micro-indentation techniques were carried out on the cross-sections to measure elastic modulus, hardness, and fracture toughness. OM and SEM microscopy were used to measure the size and shape of the indentations, the state, evolution, and morphology of the cracks; and the general structural aspects of the ceramic coating. The fracture toughness (K_{1C}) of the TC was evaluated with the James Lankford model.

$$K_{1c} = 0.0363 \left(\frac{E}{H}\right)^{\frac{2}{3}} \left(\frac{P}{a^{1.5}}\right) \left(\frac{a}{c}\right)^{1.56}$$

A method employing Weibull statistics was applied to evaluate results from K_{1C} values:

$$P(K_{1c}) = 1 - e^{-\left(\frac{K_{1c}}{K_0}\right)^m}$$

where m, is the Weibull modulus, and K_0 is the characteristic fracture toughness.

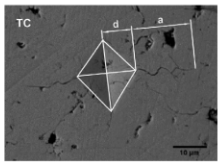

Fig. 2. Vickers indentation of a heat treated sample (1100°C, 1700 h).

Results

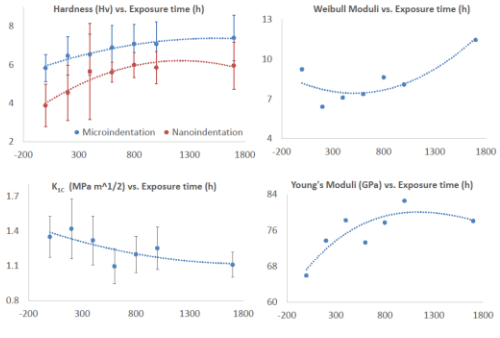

Fig. 3. Hardness, fracture toughness, Weibull and Young's moduli of TBCs, at 1100ºC at different times.

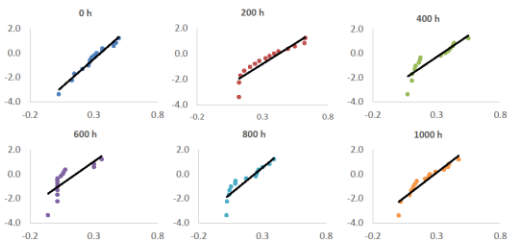

Fig. 4. Weibull plots for fracture toughness - $ln\ln(1/(1-P(K1c)))$ vs lnK_{1c}.

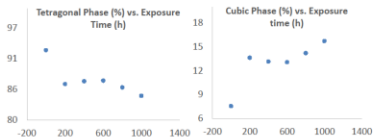

Fig. 5. Quantification of tetragonal and cubic phases by Rietveld method [2].

Time (h)	m	K_0
0	9.2	26.0
200	6.4	15.0
400	7.1	11.5
600	7.4	3.2
800	8.6	12.9
1000	8.1	9.9
1700	11.4	5.5

Table 1. Weibull parameters at different exposure times.

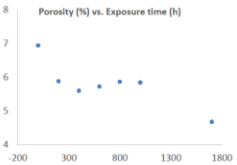

Fig. 6. Porosity content vs. Exposure time [2].

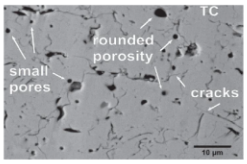

Fig. 7. Cross-section of the TC heat treated sample at 1100°C during 1700 h.

Conclusions

- From 0 up to 600 hours of heat treatment, before the formation of the monoclinic phase, hardness and Young's modulus of the TC rapidly grew up; this is explained by the sintering phenomena. Further from the 600 hours, the hardness continued growing up, but the young's modulus got to a steady state due to competition between sintering mechanism and phase transformations (where sintering tried to augment E and phase transformation tried to reduce it).
- The fracture toughness decreased with exposition time up to 23% showing a detriment of the ceramic layer. The Lankford Model gave results similar to those found in the literature for the 6-8 wt.% YSZ, showing a reliable method.
- After indentations, the direction in which radial cracks spread was ruled by the TC microstructure (parallel to the TC/TGO).
- In general K1c data follows the Weibull's equation. However, between 400 and 600°C, the data do not conform with weibulll´s equation due to their scatteredness; this can be explained by the fact that the material undergoes structural transformation that is caused by phase changes, sintering , and evolution of residual stresses.
- The IF method, in conjunction with failure statistics, has proven to be a powerful tool for the assessment of the microstructural behavior, showing the trend of the densification due to sintering.

ACKNOWLEDGEMENTS

The authors wish to acknowledge the opportunity to participate in the **Nanomechanical Testing in Materials Research and Development V** (An ECI Conference Series). The results presented herein were possible thanks to the financial support given by Empresas Públicas de Medellín, EPM, through their project *"Protección y Recuperación de Componentes de la Ruta de Gases Calientes de Turbinas a Gas Clase F Mediante Aplicación de Revestimientos de Barrera Térmica – TBC"*, by Universidad Nacional de Colombia, and by the Laboratorio de Tribología y Superficies.

Contact

Carlos Serna
Universidad Nacional de Colombia
Email: cmsernaz@unal.edu.co
Phone: 57-3044235586

References

1. N. P. Padture, "Thermal Barrier Coatings for Gas-Turbine Engine Applications," Science (80-.)., vol. 296, no. 5566, pp. 280–284, Apr. 2002.
2. J. D. Osorio, D. Maya, A. C. Barrios, A. Lopera, F. Jiménez, J. M. Meza, J. P. Hernández-Ortiz, and A. Toro, "Correlations between microstructure and mechanical properties of air plasma-sprayed thermal barrier coatings exposed to a high temperature," J. Am. Ceram. Soc., vol. 96, no. 12, pp. 3901–3907, 2013.
3. A. G. Evans and J. W. Hutchinson, "The thermomechanical integrity of thin films and multilayers," Acta Metall. Mater., vol. 43, no. 7, pp. 2507–2530, Jul. 1995.
4. J. Lankford, "Indentation microfracture in the Palmqvist crack regime: Implications for fracture toughness evaluation by the indentation method," J. Mater. Sci. Lett., vol. 1, no. 11, pp. 493–495, Nov. 1982.
5. M. Cinibiz, E. Canli, H. Kose, M. S. Salman, and O. Solmaz, "Ceramic Coating Applications and Research Fields for Internal Combustion Engines," in Ceramic Coatings - Applications in Engineering, INTECH Open Access Publisher, 2012, pp. 195–234.
6. A. Rico, J. Gómez-García, C. J. Múnez, P. Poza, and V. Utrilla, "Mechanical properties of thermal barrier coatings after isothermal oxidation. Depth sensing indentation analysis," Surf. Coatings Technol., vol. 203, no. 16, pp. 2307–2314, 2009.
7. C. Lu, R. Danzer, and F. D. Fischer, "Fracture statistics of brittle materials: Weibull or normal distribution," Phys. Rev. E - Stat. Nonlinear, Soft Matter Phys., vol. 65, no. 6, pp. 1–4, 2002.
8. C. D. Lai, Generalized Weibull Distributions. Springer, 2014.
9. A. Dey, A. K. Mukhopadhyay, S. Gangadharan, M. K. Sinha, and D. Basu, "Weibull modulus of nano-hardness and elastic modulus of hydroxyapatite coating," J. Mater. Sci., vol. 44, no. 18, pp. 4911–4918, 2009.

C. Appendix: Rietveld refinement

Next, are presented the single steps that were used for the Rietveld refinement of the diffractograms using the software HighScore Plus 3.0c; The database COD[10] was used for the phase identification. The Rietveld refinement was performed using the semi-automatic refinement mode in the software. These steps were based upon the training presentations[11] for X-ray facilities of the Center for Materials Science and Engineering of the Massachusetts Institute of Technology, MIT.

Rietveld refinement steps:

(1.1) Background fitting (polynomial): Granularity 7, bending factor 1.
(1.2) Searching peaks.
(1.3) Finding reference parameters from the COD (search and match).
(1.4) Setting refinement to semi-automatic mode and converting COD patterns to phases.

(2.1) Refinement of Scale Factors only.

(2.2) Refinement of Flat Background.

(2.3) Refinement of Flat Background + Coefficient 1.

(2.4) Refinement of Flat Background + Coefficient 1 + Coefficient 2 + Coefficient 3.

(2.5) Refinement of Flat Background + Coefficient 1 + Coefficient 2 + Coefficient 3 + Coefficient 4.

[10] http://www.crystallography.net/cod/
[11] http://prism.mit.edu/xray/education/downloads.html

(2.6) Refinement of Flat Background + Coefficient 1 + Coefficient 2 + Coefficient 3 + Coefficient 4 + 1/X Background.
(2.7) Refinement of previous parameters + specimen displacement.
(2.8) Refinement of previous parameters - specimen displacement + zero shift (2theta).

Keeping all previous parameters:
(3.1) Refinement of Cagliotti parameters one at a time (W only, V only and U only)
(3.2) Refinement of Peak Shape 1 (not refining any Cagliotti parameters)
(3.3) Refinement of asymmetry (Rietveld).
(3.4) Repeat (3.1) and (3.2) at least three times.

(4.1) Refinement of unit cell parameters.
(4.2) Refinement of W.
(4.3) Refinement of W +V.
(4.4) Refinement of W +V + U.
(4.5) Refinement of W +V + U + Peak Shape 1.
(4.6) Repeat (4.2) up to (4.5) at least 3 times.

To evaluate the quality of the refinement, the Weighted R profile should be less than 10% and as close to the R expected value as possible; R expected is an estimation of the best possible R profile based on the statistical noise of the experimental diffraction pattern.

D. Appendix: Micrographic panoramas

In order to have a good comparison between failure at room temperature and elevated temperature after the tensile test, the AT-13 (110) and AT-13 (140) coatings were loaded beyond the critical strain (A), up to (C).

Microscopic panoramas are shown of the (C) stage are shown below.

Cracking stage C

AT-13 (110) at high temperature

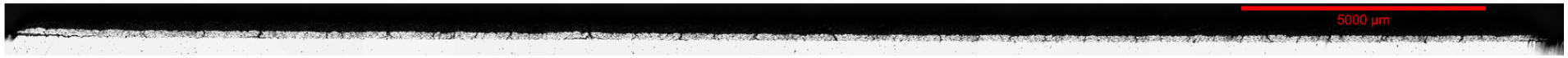

AT-13 (110) at room temperature

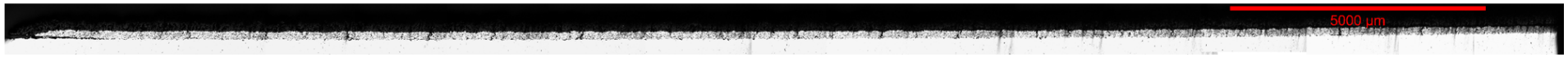

AT-13 (140) at high temperature

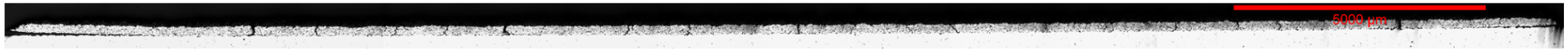

AT-13 (140) at room temperature

References

[1] F. Shi, *CERAMIC COATINGS - APPLICATIONS IN ENGINEERING*. 2012.

[2] Scopus, “Scopus,” 2016. [Online]. Available: http://www.scopus.com/. [Accessed: 01-Jan-2015].

[3] W. N. Harrison, D. G. Moore, and J. C. Richmond, “Review of an investigation of ceramic coatings for metallic turbine parts and other high-temperature applications,” techreport, 1947.

[4] R. C. Reed, *The Superalloys, Fundamentals and Applications*. 2006.

[5] H. Aleksanoglu, A. Scholz, M. Oechsner, C. Berger, M. Rudolphi, M. Schütze, and W. Stamm, “Determining a critical strain for APS thermal barrier coatings under service relevant loading conditions,” *Int. J. Fatigue*, vol. 53, pp. 40–48, 2013.

[6] Astm, “E8/E8M standard test methods for tension testing of metallic materials 1,” *Annu. B. ASTM Stand. 4*, no. C, pp. 1–27, 2010.

[7] P. Bansal, N. P. Padture, and A. Vasiliev, “Improved interfacial mechanical properties of Al2O3-13wt%TiO2 plasma-sprayed coatings derived from nanocrystalline powders,” *Acta Mater.*, vol. 51, no. 10, pp. 2959–2970, 2003.

[8] I. M. Kusoglu, E. Celik, H. Cetinel, I. Ozdemir, O. Demirkurt, and K. Onel, “Wear behavior of flame-sprayed Al2O3–TiO2 coatings on plain carbon steel substrates,” *Surf. Coatings Technol.*, vol. 200, no. 1–4, pp. 1173–1177, 2005.

[9] M. Ciniviz, E. Canli, H. Kose, M. S. Salman, and O. Solmaz, “Ceramic Coating Applications and Research Fields for Internal Combustion Engines,” in *Ceramic Coatings - Applications in Engineering*, INTECH Open Access Publisher, 2012, pp. 195–234.

[10] M. Gell, L. Xie, X. Ma, E. H. Jordan, and N. P. Padture, “Highly durable thermal barrier coatings made by the solution precursor plasma spray process,” *Surf. Coatings Technol.*, vol. 177, pp. 97–102, 2004.

[11] P. L. Fauchais, J. V. R. Heberlein, and M. I. Boulos, *Thermal Spray Fundamentals*. 2014.

[12] H. Wang, Y. Luo, P. Friedman, M. Chen, and L. Gao, “Warm forming behavior of high strength aluminum alloy AA7075,” *Trans. Nonferrous Met. Soc. China*, vol. 22, no. 1, pp. 1–7, 2012.

[13] T. Stoltenhoff, F. Zimmermann, K. Gorris, and H. Burger, “Process for the repair and restoration of dynamically stressed components comprising aluminium alloys for aircraft applications,” 2007.

[14] E. Heinonen-Person, “Method of surface treating high-strength aluminum,” 2001.

[15] P. Cavaliere and A. Squillace, “High temperature deformation of friction stir processed 7075 aluminium alloy,” *Mater. Charact.*, vol. 55, no. 2, pp. 136–142,

2005.

[16] D. T. Macedo, L. B. Cruvinel, and L. C. Casteletti, “AVALIAÇÃO DE REVESTIMENTOS PRODUZIDOS POR ASPERSÃO TÉRMICA EM SUBSTRATO DA LIGA DE ALUMINIO 7075–T3,” in *CONGRESSO BRASILEIRO DE ENGENHARIA E CIÊNCIA DOS MATERIAIS*, 2006, vol. 17.

[17] B. Arsenault, P. Gougeon, M. Verdier, and D. L. Duquesnay, “Aluminum protective coatings - Fatigue and bond strength properties with respect to surface preparation techniques: Laser ablation, shot peening and grit blasting,” *Can. Metall. Q.*, vol. 45, no. 1, pp. 49–58, 2006.

[18] C. Mourad, S. Tahar, B. Wassila, and M. Nadia, “Propriétés Microstructurales du Revêtement Cr3 C 2-NiCr Obtenu par Projection HVOF,” in *Conférence Internationale sur le Soudage, le CND et l’Industrie des Métaux, IC-WNDT-MI’10*, 2010.

[19] M. Barbosa, N. Cinca, S. Dosta, and J. M. Guillemany, “Cold Spray Deposition of Titanium onto Aluminium Alloys,” *Ciência Tecnol. dos Mater.*, vol. 22, no. 1–2, pp. 48–56, 2010.

[20] K. Ambiger and A. Kumar, “ANTI-WEAR BEHAVIOUR OF PLASMASPRAYED ALUMINA & ZIRCONIA COATINGS ON ALUMINIUM 7075T6,” *Int. J. Tech. Res. Appl.*, vol. 2, no. 4, pp. 235–241, 2014.

[21] Ş. Yılmaz, M. Ipek, G. F. Celebi, and C. Bindal, “The effect of bond coat on mechanical properties of plasma-sprayed Al2O3 and Al2O3–13wt% TiO2 coatings on AISI 316L stainless steel,” *Vacuum*, vol. 77, no. 3, pp. 315–321, 2005.

[22] S. Guessasma, M. Bounazef, P. Nardin, and T. Sahraoui, “Wear behavior of alumina-titania coatings: Analysis of process and parameters,” *Ceram. Int.*, vol. 32, no. 1, pp. 13–19, 2006.

[23] a. Rico, P. Poza, and J. Rodríguez, “High temperature tribological behavior of nanostructured and conventional plasma sprayed alumina-titania coatings,” *Vacuum*, vol. 88, no. 1, pp. 149–154, 2013.

[24] R. S. Lima and B. R. Marple, “Superior Performance of High-Velocity Oxyfuel-Sprayed Nanostructured TiO2 in Comparison to Air Plasma-Sprayed Conventional Al2O3-13TiO2,” *J. Therm. Spray Technol.*, vol. 14, no. 3, pp. 397–404, Sep. 2005.

[25] N. Cinca, C. R. C. Lima, and J. M. Guilemany, “An overview of intermetallics research and application: Status of thermal spray coatings,” *J. Mater. Res. Technol.*, vol. 2, no. 1, pp. 75–86, 2013.

[26] R. Younes, M. A. Bradai, A. Sadeddine, Y. Mouadji, A. Bilek, and A. Benabbas, “Microstructural and Tribological Properties of Al2O3-13pctTiO2 Thermal Spray Coatings Deposited by Flame Spraying,” *Metall. Mater. Trans. B*, vol. 46, no. 5, pp. 2394–2403, 2015.

[27] M. Roy and J. P. Davim, Eds., *Thermal Sprayed Coatings and their Tribological Performances*. IGI Global, 2015.

[28] N. Espallargas, *Future Development of Thermal Spray Coatings*. Elsevier, 2015.

[29] F. Vargas, “Élaboration de couches céramiques épaisses à structures micrométriques et anométriques par projections thermiques pour des applications tribologiques,” Ph.D. Thesis, Limoges, 2010.

[30] G. Bolelli, V. Cannillo, L. Lusvarghi, and T. Manfredini, “Wear behaviour of thermally sprayed ceramic oxide coatings,” *Wear*, vol. 261, no. 11–12, pp. 1298–1315, 2006.

[31] J. R. Davis and others, *Handbook of thermal spray technology*. ASM international, 2004.

[32] M. Kelly, J. Singh, J. Todd, S. Copley, and D. Wolfe, “Metallographic techniques for evaluation of Thermal Barrier Coatings produced by Electron Beam Physical Vapor Deposition,” *Mater. Charact.*, vol. 59, no. 7, pp. 863–870, 2008.

[33] Y. Tamarin, *Protective coatings for turbine blades*. ASM international, 2002.

[34] I. G. Cano, S. Dosta, J. R. Miguel, and J. M. Guilemany, “Production and characterization of metastable Al2O3–TiO2 ceramic materials,” *J. Mater. Sci.*, vol. 42, no. 22, pp. 9331–9335, Sep. 2007.

[35] R. S. Lima, C. Moreau, and B. R. Marple, “HVOF-Sprayed coatings engineered from mixtures of nanostructured and submicron Al 2O 3-TiO 2 powders: An enhanced wear performance,” *J. Therm. Spray Technol.*, vol. 16, no. December, pp. 866–872, 2007.

[36] A. Queen, “‘Mechanics of components with treated or coated surfaces’ by Jaraslav Mencik,” *Strain*, vol. 33, no. 3, pp. 101–101, Aug. 1997.

[37] P. Scardi, M. Leoni, L. Bertamini, and M. Marchese, “Residual stress in plasma sprayed Y2O3-PSZ coatings on piston heads,” *Surf. Coatings Technol.*, vol. 86–87, no. PART 1, pp. 109–115, 1996.

[38] M. Shinozaki, “The effect of sintering and CMAS on the stability of plasma-sprayed zirconia thermal barrier coatings,” University of Cambridge, 2013.

[39] S. Kuroda, T. Dendo, and S. Kitahara, “Quenching stress in plasma sprayed coatings and its correlation with the deposit microstructure,” *J. Therm. Spray Technol.*, vol. 4, no. 1, pp. 75–84, Mar. 1995.

[40] Y. Wang, W. Tian, T. Zhang, and Y. Yang, “Microstructure, spallation and corrosion of plasma sprayed Al2O3–13%TiO2 coatings,” *Corros. Sci.*, vol. 51, no. 12, pp. 2924–2931, Dec. 2009.

[41] A. G. Evans and J. W. Hutchinson, “The thermomechanical integrity of thin films and multilayers,” *Acta Metall. Mater.*, vol. 43, no. 7, pp. 2507–2530, Jul. 1995.

[42] W. Zhu, L. Yang, J. W. Guo, Y. C. Zhou, and C. Lu, “Numerical study on interaction of surface cracking and interfacial delamination in thermal barrier coatings under tension,” *Appl. Surf. Sci.*, vol. 315, pp. 292–298, 2014.

[43] C. B. Carter and M. G. Norton, *Ceramic materials: science and engineering*. Springer Science & Business Media, 2007.

[44] V. Postolenko, “Failure Mechanisms of Thermal Barrier Coatings for High Temperature Gas Turbine Components under Cyclic Thermal Loading,” Fachgruppe für Metallurgie und Werkstofftechnik, 2008.

[45] A. Shinmi, “Characterization of the materials used in air plasma sprayed thermal barrier coatings,” The University of Manchester, 2011.

[46] D. Wu, A. Mezrin, B. Sachek, V. Sakharov, and N. Frolov, “Interface Fracture Toughness Of TBCs At High Temperature,” in *ICF11, Italy 2005*, 2013.

[47] W. G. Mao, C. Y. Dai, L. Yang, and Y. C. Zhou, “Interfacial fracture characteristic and crack propagation of thermal barrier coatings under tensile conditions at

elevated temperatures," *Int. J. Fract.*, vol. 151, no. 2, pp. 107–120, 2008.

[48] B. N. Jaya and Z. Alam, "Small-scale mechanical testing of materials," *Curr. Sci.*, vol. 105, no. 8, p. 27, 2013.

[49] N. K. Fukumasu, C. M. Angelo, M. Ignat, and R. M. Souza, "Numerical study of tensile tests conducted on systems with elastic-plastic films deposited onto elastic-plastic substrates," *Surf. Coatings Technol.*, vol. 205, no. 5, pp. 1415–1419, 2010.

[50] M. Zhou, W. B. Yao, X. S. Yang, Z. B. Peng, K. K. Li, C. Y. Dai, W. G. Mao, Y. C. Zhou, and C. Lu, "In-situ and real-time tests on the damage evolution and fracture of thermal barrier coatings under tension: A coupled acoustic emission and digital image correlation method," *Surf. Coatings Technol.*, vol. 240, pp. 40–47, 2014.

[51] C. Eberl, D. S. Gianola, X. Wang, M. Y. He, a. G. Evans, and K. J. Hemker, "A method for in situ measurement of the elastic behavior of a columnar thermal barrier coating," *Acta Mater.*, vol. 59, no. 9, pp. 3612–3620, 2011.

[52] B. Zhou and K. Kokini, "Effect of pre-existing surface crack morphology on the interfacial thermal fracture of thermal barrier coatings. A numerical study," *Mater. Sci. Eng. A*, vol. 348, no. 1–2, pp. 271–279, 2003.

[53] L. Qian, S. Zhu, Y. Kagawa, and T. Kubo, "Tensile damage evolution behavior in plasma-sprayed thermal barrier coating system," *Surf. Coatings Technol.*, vol. 173, no. 2–3, pp. 178–184, 2003.

[54] W. D and Z. Y. C, "Interface fracture toughness of TBCs at high temperature," *Int. Conf. Fract.*, 2005.

[55] R. B. Abernethy, *The New Weibull Handbook*. RB Abernethy, 1996.

[56] A. C. Fischer-Cripps, *Introduction To Contact Mechanics*. 2007.

[57] R. Documents, "Standard Practice for Reporting Uniaxial Strength Data and Estimating Weibull Distribution Parameters for Advanced Ceramics 1," *Order A J. Theory Ordered Sets Its Appl.*, vol. i, no. January, pp. 1–24, 2001.

[58] H. Boyer, *Atlas of Stress--strain Curves*, 2nd. 1987.

[59] D. G. Puerta, "The development and characterization of electrochemically processed thermal barrier coatings," article, Lehigh University, 1998.

[60] D. G. Puerta, "Accepted Practices of Thermal Spray Technology: Sectioning," *J. Therm. Spray Technol.*, vol. 15, no. 1, pp. 31–32, 2006.

[61] W. J. Brindley and T. a. Leonhardt, "Metallographic techniques for evaluation of thermal barrier coatings," *Materials Characterization*, vol. 24, no. 2. pp. 93–101, 1990.

[62] D. Puerta, J. Sabine, and a Geary, "Metallographic Characterization of Thermal Spray Microstructures," *Microsc. Microanal.*, vol. 12, no. S02, p. 1602, 2006.

[63] D. G. Puerta, "Accepted Practices of Thermal Spray Technology: Fine Grinding and Polishing," *J. Therm. Spray Technol.*, vol. 15, no. 1, pp. 31–32, 2006.

[64] D. G. Puerta, "Accepted Practices of Thermal Spray Technology: Grinding," *J. Therm. Spray Technol.*, vol. 15, no. 1, pp. 31–32, 2006.

[65] D. G. Puerta, "Accepted Practices of Thermal Spray Technology: Mounting," *J. Therm. Spray Technol.*, vol. 15, no. 1, pp. 31–32, 2006.

[66] S. S. Singh, J. J. Loza, A. P. Merkle, and N. Chawla, “Three dimensional microstructural characterization of nanoscale precipitates in AA7075-T651 by focused ion beam (FIB) tomography,” *Mater. Charact.*, vol. 118, pp. 102–111, Aug. 2016.

[67] G. E. Totten and D. S. Mackenzie, *Handbook of Aluminum: Volume 2: Alloy Production and Materials Manufacturing*. 2003.

[68] K. a. Habib, J. J. Saura, C. Ferrer, M. S. Damra, E. Giménez, and L. Cabedo, “Comparison of flame sprayed Al2O3/TiO2 coatings: Their microstructure, mechanical properties and tribology behavior,” *Surf. Coatings Technol.*, vol. 201, no. 3–4, pp. 1436–1443, 2006.

[69] F. Vargas, H. Ageorges, P. Fournier, P. Fauchais, and M. E. López, “Mechanical and tribological performance of Al2O3-TiO2 coatings elaborated by flame and plasma spraying,” *Surf. Coatings Technol.*, vol. 205, no. 4, pp. 1132–1136, 2010.

[70] M. Uma Devi, “New phase formation in Al2O3-based thermal spray coatings,” *Ceram. Int.*, vol. 30, no. 4, pp. 555–565, 2004.

[71] J. H. She and T. Ohji, “Fabrication and characterization of highly porous mullite ceramics,” *Mater. Chem. Phys.*, vol. 80, no. 3, pp. 610–614, 2003.

[72] A. S. Wagh, J. P. Singh, and R. B. Poeppel, “Dependence of ceramic fracture properties on porosity,” *J. Mater. Sci.*, vol. 28, no. 13, pp. 3589–3593, 1993.

[73] L. Yang, Z.-C. Zhong, Y.-C. Zhou, and C.-S. Lu, “Quantitative assessment of the surface crack density in thermal barrier coatings,” *Acta Mech. Sin.*, vol. 30, no. 2, pp. 167–174, 2014.